SIGNAL TRANSDUCTION

MCJ: A mitochondrial target for cardiac intervention in pulmonary hypertension

Ayelén M. Santamans[1], Beatriz Cicuéndez[1], Alfonso Mora[1,2], María Villalba-Orero[1,3], Sanela Rajlic[4,5], María Crespo[1], Paula Vo[6], Madison Jerome[6], Álvaro Macías[1], Juan Antonio López[7,8], Magdalena Leiva[9], Susana F. Rocha[1], Marta León[1], Elena Rodríguez[1,2], Luis Leiva[1,2], Aránzazu Pintor Chocano[1], Inés García Lunar[1,7,10], Ana García-Álvarez[1,7,11], Pablo Hernansanz-Agustín[12], Víctor I. Peinado[13,14,15], Joan Albert Barberá[14,15], Borja Ibañez[1,7,16], Jesús Vázquez[7,8], Jessica B. Spinelli[6,17], Andreas Daiber[4,18], Eduardo Oliver[1,7,19], Guadalupe Sabio[1,2]*

Pulmonary hypertension (PH) can affect both pulmonary arterial tree and cardiac function, often leading to right heart failure and death. Despite the urgency, the lack of understanding has limited the development of effective cardiac therapeutic strategies. Our research reveals that MCJ modulates mitochondrial response to chronic hypoxia. MCJ levels elevate under hypoxic conditions, as in lungs of patients affected by COPD, mice exposed to hypoxia, and myocardium from pigs subjected to right ventricular (RV) overload. The absence of MCJ preserves RV function, safeguarding against both cardiac and lung remodeling induced by chronic hypoxia. Cardiac-specific silencing is enough to protect against cardiac dysfunction despite the adverse pulmonary remodeling. Mechanistically, the absence of MCJ triggers a protective preconditioning state mediated by the ROS/mTOR/HIF-1α axis. As a result, it preserves RV systolic function following hypoxia exposure. These discoveries provide a potential avenue to alleviate chronic hypoxia-induced PH, highlighting MCJ as a promising target against this condition.

INTRODUCTION

Pulmonary hypertension (PH), characterized by elevated blood pressure within the pulmonary arteries (PAs), emerges as an important concern for patients with chronic lung conditions such as idiopathic pulmonary fibrosis, chronic obstructive pulmonary disease (COPD), and individuals residing at high altitudes. This association underscores a notable risk, as the chronic hypoxic exposure inherent to these groups accentuates the likelihood of PH development, as supported by multiple studies (*1*–*3*). These patients exhibit distinct characteristics, including extensive remodeling of the pulmonary vascular network and elevated PA pressure, which leads to right ventricular (RV) pressure overload (*4*). While substantial progress has been made in understanding and treating PA remodeling and vasoconstriction, existing treatments mainly focus on targeting the pulmonary vascular tone. However, these therapies only mitigate some symptoms as this disease remains without cure, and many patients still succumb to heart failure (*5*, *6*). Consequently, it is essential to gain a deeper understanding of the cardiac molecular mechanisms involved in PH.

Notably, the main cause of morbidity and mortality in patients with PH is RV remodeling followed by heart failure. Some evidence shows that PH outcome is more faithfully predicted by the capacity of the RV to adapt to the pressure overload, shifting the focus of research efforts to therapeutic strategies targeting the heart (*7*). It remains unclear whether cardiac tissue senses decreases in O_2 availability and how this might affect the cardiac outcome in PH (*8*, *9*). Recent studies reported a reduction in RV O_2 supply during PH, suggesting that cardiac hypoxic adaptation might be a crucial determinant of PH progression (*10*, *11*).

Hypoxia triggers molecular adaptive responses within cardiac mitochondria (*12*). These adaptations aim to optimize energy production under limited oxygen conditions to ensure an uninterrupted contractile function of the heart. Thus, understanding the interplay between mitochondrial function and hypoxic challenges is essential to elucidate the mechanistic framework responsible for cardiac resilience and vulnerability.

Methylation-controlled J protein (MCJ; encoded by the nuclear gene *DNAJC15*) is a small, 150–amino acid protein in the inner mitochondrial membrane that modulates mitochondrial metabolism by regulating complex I (CI) activity and oxidative stress (*13*–*16*). MCJ expression is primarily regulated through CpG island methylation within its promoter (*17*). In the liver, is suggested to have evolved as a regulator of CI function, acting as a brake under challenging metabolic conditions that substantially affect mitochondrial function, such as nutrient excess or depletion (*15*, *16*). While MCJ function in

[1]Cardiovascular Risk Factors and Brain Function Program, Centro Nacional de Investigaciones Cardiovasculares (CNIC), Madrid, Spain. [2]Molecular Oncology Programme, Organ crosstalk in metabolic diseases group, Centro Nacional de Investigaciones Oncológicas (CNIO), Madrid, Spain. [3]Departamento de Medicina y Cirugía Animal, Facultad de Veterinaria, Universidad Complutense de Madrid, Madrid, Spain. [4]Department of Cardiothoracic and Vascular Surgery, University of Medicine Mainz, 55131 Mainz, Germany. [5]Department of Cardiology, Department of Cardiology, Molecular Cardiology, University Medical Center, 55131 Mainz, Germany. [6]Program in Molecular Medicine, UMass Chan Medical School, Worcester MA 01605. [7]CIBER de Enfermedades Cardiovasculares (CIBERCV), Madrid, Spain. [8]Novel mechanisms of Atherocleroclerosis Program, Centro Nacional de Investigaciones Cardiovasculares (CNIC), Madrid, Spain. [9]Department of Immunology, School of Medicine, Complutense University of Madrid, Madrid, Spain. [10]Cardiology Department, University Hospital La Moraleja, Madrid, Spain. [11]Cardiology Department, Hospital Clínic Barcelona-IDIBAPS, University of Barcelona, Barcelona, Spain. [12]Cardiovascular Regeneration Program, Centro Nacional de Investigaciones Cardiovasculares (CNIC), Madrid, Spain. [13]Department of Experimental Pathology, Instituto de Investigaciones Biomédicas de Barcelona (IIBB-CSIC-IDIBAPS), Barcelona, Spain. [14]Department of Pulmonary Medicine, Hospital Clínic, Institut d'Investigacions Biomèdiques August Pi i Sunyer (IDIBAPS), University of Barcelona, Barcelona, Spain. [15]Biomedical Research Networking Center on Respiratory Diseases (CIBERES), Madrid, Spain. [16]Cardiology Department, IIS-Fundación Jiménez Díaz Hospital, Madrid, Spain. [17]UMass Chan Medical School Cancer Center, Worcester MA 01605. [18]German Center for Cardiovascular Research (DZHK), Partner Site Rhine-Main, 55131 Mainz, Germany. [19]Centro de Investigaciones biológicas Margarita Salas (CIB-CSIC), Madrid, Spain.
*Corresponding author. Email: gsabio@cnic.es

regulating these processes is well established (*13*, *14*, *16*, *18*–*21*), its potential role in modulating mitochondrial responses to low oxygen levels, a critical challenge for cardiomyocyte mitochondria, remains unexplored.

Our investigation unveils the important role of MCJ in cardiomyocyte responses to chronic hypoxia. MCJ levels rise under hypoxic conditions, such as in human lungs afflicted with COPD, lungs and myocardium from mice exposed to hypoxia, and pigs subjected to RV pressure overload. Without MCJ, the RV function is preserved, safeguarding against both cardiac and lung remodeling caused by chronic hypoxia. By exclusively depleting MCJ in cardiomyocytes, we successfully dissociate the pulmonary state from the cardiac outcome. Mechanistically, the absence of MCJ is associated with increased baseline reactive oxygen species (ROS), which triggers the mammalian target of rapamycin (mTOR)/hypoxia-inducible factor–1α (HIF-1α) axis. This pathway acts like a protective preconditioning state that conserves the RV systolic function after hypoxia exposure. These findings provide a potential therapeutic target against the RV systolic dysfunction derived from PH, suggesting that cellular adaptation to hypoxia may protect against the deathly consequences of PH.

RESULTS

MCJ expression in lungs of patients with COPD and myocardium of pigs is enhanced after RV pressure overload

To investigate the potential implication of MCJ in hypoxia-related diseases, we measured its expression in lung tissue from patients with COPD, a condition characterized by alveolar hypoxia (*22*). We observed a trend for MCJ expression to be positively correlated with higher values on the BODE index (body mass index, airflow obstruction, dyspnea, and exercise capacity), a predictor of the number and severity of acute COPD exacerbations (Fig. 1A) (*23*). Moreover, MCJ expression was associated with a low diffusing capacity of the lung for carbon monoxide (DLCO) (Fig. 1A). A reduced DLCO is commonly indicative of pulmonary vascular disease (*24*), denoting impaired ability of the lungs to transfer gas from inspired air to the bloodstream. Patients with COPD are at risk of developing PH with RV heart failure, which is associated with increased mortality risk (*25*, *26*). Induction of RV pressure overload in pigs upon surgical restrictive banding of the main PA increased MCJ RNA and protein expression in the RV myocardium (Fig. 1B). Consistent with this finding, chronic hypoxia in mice induced an up-regulation of MCJ expression in the heart and lung tissues (Fig. 1C). These results support a role of MCJ both in the pulmonary bed during PH and in secondary RV involvement after pressure overload.

MCJ depletion confers protection against PH induced by chronic hypoxia

To investigate the implication of MCJ in the development of PH and associated RV dysfunction induced by chronic hypoxia, we took advantage of MCJ whole-body knockout (MCJ^{KO}) mice (Fig. 1D). Echocardiography detected RV hypertrophy and decreased RV function in wild-type (WT) mice in these hypoxic conditions, whereas MCJ^{KO} mice showed no signs of hypertrophy and preserved their RV function (Fig. 1, E and F). These findings were further corroborated through quantification of RV cross-sectional area and the Fulton index (fig. S1, A and B). MCJ^{KO} mice presented no signs of RV dilation or altered left ventricle (LV) geometry under hypoxic conditions (fig. S1, C and D). This contrasted with WT mice, where a reduction in LV cavity volume was observed, possibly caused by displacement of the interventricular septum by the enlarged RV (*27*). However, as expected, hypoxia had no impact on LV function in none of the models (fig. S1E). These data indicated that MCJ^{KO} mice were protected from the morphological and functional effects induced by chronic hypoxia.

RV systolic pressure (RVSP), a surrogate of pulmonary arterial pressure, indicated that only WT mice developed PH after chronic hypoxia (Fig. 1G). Alveolar hypoxia triggers lung vasculature remodeling, vasoconstriction, and lung inflammation, which progress to PH (*28*–*32*). WT mice subjected to chronic hypoxia displayed an augmented density of muscularized vessels, characterized by extensive structural alterations in the vascular wall and infiltration of macrophages and neutrophils within the lungs. Remodeling was absent in MCJ^{KO} mice, which also showed less inflammation (Fig. 1, H and I). It is important to highlight that the baseline infiltration and M1/M2 polarization markers exhibited almost no differences between WT and MCJ^{KO} lungs (figs. S2, A and B, and S3). Moreover, the distinct infiltration patterns between the two genotypes might be attributed to slight variations in secretory cytokine profiles (fig. S4). In addition, a bone marrow transplantation experiment ruled out immune cell involvement in the cardiac phenotype (fig. S5). In addition, we found that hypoxia-exposed MCJ^{KO} mice had less PA vasoconstriction than similarly treated WT mice, suggesting a cell-type–specific role of MCJ in pulmonary vessels (fig. S6A). MCJ expression is higher in endothelial cells (EC) than in vascular smooth muscle cells (VSMCs) (fig. S6, B and C), a finding consistent with myography analysis showing that MCJ contributed to the sustained, EC-dependent phase of PH (phase II), but not to the acute, VSMC-dependent phase (phase I) (fig. S6A) (*33*, *34*). These results indicate that MCJ deficiency specifically affects the endothelium, leaving the vascular component unaltered. The EC-restricted effect also accounts for the persistence of residual PA vasoconstriction despite the lack of MCJ reducing the amplitude of the sustained phase of acute hypoxic pulmonary vasoconstriction. Together, these results show that lack of MCJ protects against pulmonary and RV damage induced by chronic hypoxia.

To extend our findings into a more severe PH context, we combined Sugen 5416 treatment with hypoxia exposure (*35*). MCJ^{KO} mice demonstrated preserved RV function, despite developing RV hypertrophy and lung vessel remodeling, providing further support for MCJ modulation as a promising therapeutic avenue (fig. S7). In summary, the lack of MCJ protects against pulmonary and RV systolic dysfunction induced by chronic hypoxia.

Cardiac-specific modulation of MCJ expression determines cardiac function in hypoxia independently of lung remodeling

Current treatment strategies for PH target the pulmonary arterial vasoconstriction yet with limited success. Right heart failure stands as the primary cause of death in PH (*36*), although the lack of understanding regarding the mechanisms driving the cardiac malfunction has impeded the development of cardiac targeted interventions (*36*). While chronic hypoxia is recognized to trigger metabolic and mitochondrial adaptations in cardiac tissue (*36*–*38*), translating this knowledge into effective therapies has been hindered. Our data indicate that MCJ^{KO} mice do not develop PH following hypoxia exposure, displaying no pulmonary vascular remodeling and maintaining RV function. In consequence, the absence of lung remodeling could account for the preservation of cardiac performance. To gain a deeper insight of the specific role of MCJ in cardiomyocytes during hypoxia, we carried out two targeted experiments.

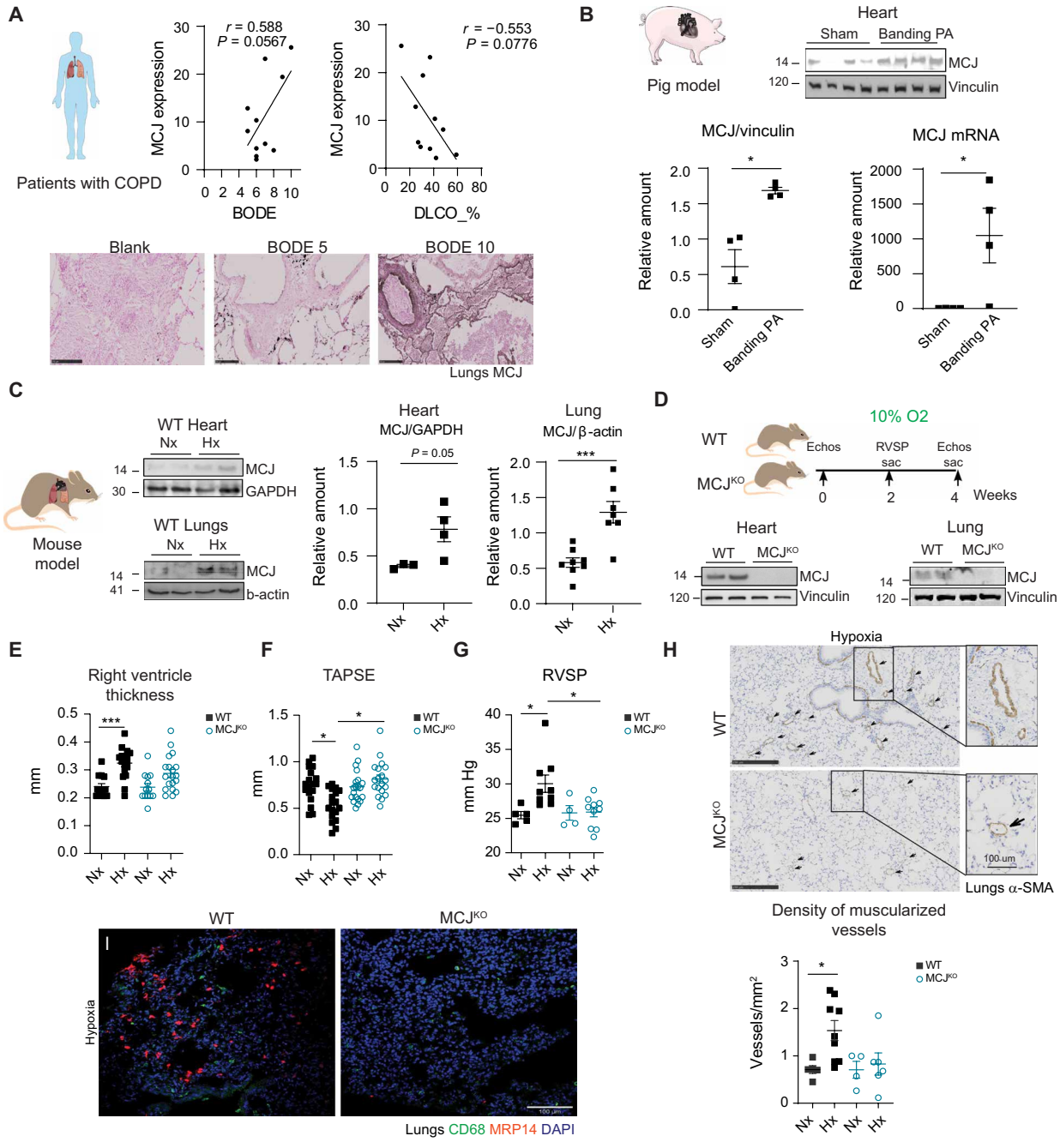

Fig. 1. MCJ deficiency protects against hypoxia-induced pulmonary hypertension. (**A**) Relation between MCJ lung expression in patients with COPD and the BODE index (body mass index, airflow obstruction, dyspnea, and exercise capacity) and the diffusing capacity of the lung for carbon monoxide (DLCO) ($n = 11$). Representative MCJ immunostaining in lung samples from patients with COPD with 5 and 10 points on the BODE index. Blank section incubated only with secondary antibody. Scale bars, 250 μm. (**B**) Swine model of chronic RV overload. MCJ protein and RNA levels were assayed by immunoblot and reverse transcription quantitative polymerase chain reaction in cardiac lysates from Yucatan pigs with surgical restrictive banding of the main PA ($n = 4$). (**C**) Representative immunoblot of cardiac and lung MCJ expression in wild-type (WT) mice maintained in normoxia (Nx; 21% O_2) or exposed to chronic hypoxia (Hx; 28 days at 10% O_2) ($n = 3$ to 8). GAPDH, glyceraldehyde-3-phosphate dehydrogenase. (**D**) Experimental scheme for (E) to (I): protocol for the analysis of lung and cardiac function in WT and MCJ^{KO} mice exposed to Nx or Hx. MCJ deletion in cardiac and lung lysates from MCJ^{KO} mice. (**E** and **F**) Echocardiography of RV hypertrophy (RV thickness) and function [tricuspid annular plane systolic excursion (TAPSE)] ($n = 18$ to 20, $N = 3$). (**G**) Right ventricular systolic pressure (RVSP) in WT and MCJ^{KO} mice ($n = 5$ to 10, $N = 2$). (**H**) Muscularized vessel density in WT and MCJ^{KO} lungs ($n = 4$ to 9, $N = 2$). Representative images show α–smooth muscle actin (α-SMA) immunostaining, amplification of a remodeled vessel in hypoxia. Scale bars, 250 μm, 100 μm (vessel). (**I**) Macrophages (CD68) and neutrophils (MRP14) infiltration in hypoxic mouse lungs. Nuclei stained with 4′,6-diamidino-2-phenylindole (DAPI). Scale bar, 100 μm. *n*, number of biological samples; *N*, number of times that the experiment was repeated. All data are presented as means ± SEM. Statistical comparison by Pearson correlation analysis (A), two-tailed Student's *t* test [(B) and (C)], or two-way analysis of variance (ANOVA) with Tukey posttest [(E) to (H)]: nonsignificant (NS), $^*P < 0.05$ and $^{***}P < 0.001$. Panels (A) to (D) prepared using modified figures from Servier Medical Art (https://smart.servier.com/), licensed under a Creative Commons Attribution 3.0 unported license.

In this context, we explored the potential role of silencing MCJ in cardiomyocytes by using an adeno-associated virus (AAV) carrying an MCJ-targeting short hairpin RNA (shRNA) under the cardiac troponin T (TNT) promoter (AAV-TNT-shMCJ) (Fig. 2, A and B, and fig. S8). Silencing MCJ specifically in cardiomyocytes effectively counteracted hypoxia-induced RV hypertrophy and dysfunction, despite sustained elevation of RVSP and associated pulmonary vascular remodeling (Fig. 2, C to E).

Next, we further evaluate the importance of cardiomyocytes in shaping cardiac outcome. To achieve cardiomyocyte-specific MCJ expression in MCJ^{KO} mice, we used AAV-overexpressing MCJ under the cardiac TNT promoter (MCJ^{KO} + TNT-MCJ) (Fig. 2, F to H). Notably, the reintroduction of MCJ specifically in MCJ^{KO} cardiomyocytes resulted in RV hypertrophy and impaired cardiac function under hypoxia in contrast to MCJ^{KO} + TNT–enhanced green fluorescent protein (EGFP), despite the absence of pulmonary vascular remodeling (Fig. 2, I and J).

Together, our results identify a cardiac-specific role of MCJ and emphasize that manipulating cardiac MCJ expression could offer a relevant approach to rescue RV systolic dysfunction, decoupled from pulmonary vessel remodeling, in various PH scenarios.

MCJ deficiency enhances ROS production, promoting mTOR activation

Under certain stimuli and in a cell-type–specific manner, MCJ might affect ROS production (*14*, *15*, *20*, *21*). Then, we investigated whether the observed cardiac protective effects in the MCJ^{KO} animals could be attributed to MCJ-mediated modulation of ROS production. Contrary to what we expected, MCJ^{KO} cardiac mitochondria presented increased basal superoxide generation assessed by mitoSOX high-performance liquid chromatography (HPLC). Furthermore, despite the heightened baseline ROS levels in the heart, these mice did not exhibit the expected increase in ROS in response to hypoxia, unlike the WT animals (Fig. 3A and fig. S9). Consistently, MitoP/MitoB ratios and quantitative redox proteomics corroborated higher ROS production in baseline MCJ^{KO} hearts (Fig. 3, B and C). Because MCJ^{KO} hearts exhibit blunted ROS responses to hypoxia, we wondered whether this may contribute to the protective phenotype. To this end, we administered the antioxidant, *N*-acetylcysteine (NAC), during 2 weeks before hypoxic exposure, to reduce the basal elevation of ROS in MCJ^{KO} hearts. The NAC treatment was deliberately stopped just before the onset of hypoxic exposure to replicate the ROS changes seen in WT animals in MCJ^{KO} hearts (Fig. 3D). MCJ^{KO} mice now displayed the development of RV hypertrophy and dysfunction under hypoxia (Fig. 3, E and F, and fig. S10, A to C). These results indicated that the increased baseline ROS levels and the impaired increase in ROS following hypoxia exposure play a role in preserving RV function in MCJ^{KO}, despite the pulmonary vascular remodeling (Fig. 3, E to H).

To comprehend the molecular mechanism underlying the preservation of the RV function in the MCJ^{KO}, we examined ROS-activated signaling pathways potentially implicated in cardiac protection. Analysis of cardiac lysates showed higher baseline activation of the mTOR pathway in MCJ^{KO} hearts, evident through the phosphorylation of S6, p70, and Akt (Fig. 4A). This activation was abrogated by NAC treatment, evidencing the role of ROS in driving mTOR activation (Fig. 4B and fig. S10D). We showed that blocking mTOR with rapamycin induced RV dysfunction in MCJ^{KO} mice, highlighting the crucial role of mTOR in cardiac protection (*39*). Although, RV hypertrophy and the density of muscularized vessels remained unaffected (Fig. 4, C to F).

These findings highlight the importance of ROS as a modulator of the mTOR pathway in the MCJ^{KO} mice and reveals a potential mechanism through which MCJ depletion leads to preservation of the RV function under hypoxia-induced stress.

mTOR activation increases HIF-1α preserving cardiac function in MCJ^{KO} under chronic hypoxia

mTOR pathway activation in normoxic conditions can stimulate the expression of HIF-1α (*40*, *41*), a pivotal transcription factor involved in hypoxic stress adaptation (*42*). Analysis of MCJ^{KO} hearts showed that HIF-1α levels and two of its downstream targets, transforming growth factor–β (TGF-β) and carbonic anhydrase IX, were already abnormally elevated in normoxia (Fig. 5, A and B), while, as expected, HIF-1α is only stabilized under hypoxia in WT hearts (Fig. 5A). Accordingly, cardiac metabolomic and its integration with proteomic data showed enrichment of metabolites associated with hypoxia-induced metabolic changes in MCJ^{KO} hearts, mainly related to altered glucose, nucleotide, and amino acid metabolism (figs. S11 and S12 and tables S1 and S2). Subsequent rapamycin treatment reinforced that this effect was mediated by the activation of the mTOR pathway under normoxia (Fig. 5C).

HIF-1α stabilization has been identified as a crucial mediator of cardioprotection through ischemic preconditioning (*43*, *44*). This prompts us to examine whether high HIF-1α expression contributes to the protection against hypoxia-induced PH in MCJ^{KO} mice. We used PX-478 to inhibit the HIF-1α pathway (*45*). We observed a notable reversal of the phenotype in the MCJ^{KO} (Fig. 5, D and E). This reversal is characterized by increased RV hypertrophy and diminished systolic function (Fig. 5, F and G). HIF-1α inhibition also showed a trend to elevate the RVSP, reduced the muscularized vessel density, and increased pulmonary inflammation, now showing the development of PH in the MCJ^{KO} (Fig. 5, H to J).

MCJ^{KO} mice exhibit activation of a pseudo-hypoxic baseline signaling, prompting us to explore its implications on the basal cardiac phenotype. MCJ^{KO} mice displayed an enlarged cross-sectional area of RV cardiomyocytes, potentially reflecting heightened mTOR pathway activation (*46*–*48*), while RV thickness and cardiac function remained normal (fig. S13, A and B). Further analysis of red blood cells (RBCs) indicated elevated mean corpuscular volume, mean corpuscular hemoglobin, and red cell distribution width in MCJ^{KO} mice (fig. S13C). Meanwhile, no inter-genotype disparities were observed in RBC count or total hemoglobin. These findings suggest that MCJ^{KO} mice have enlarged erythrocytes with an augmented capacity for hemoglobin and oxygen carriage. This observation supports the notion of a baseline pseudo-hypoxic state, potentially contributing to enhanced adaptability and improved tissue oxygen delivery in hypoxic conditions.

High ROS levels and blockade of HIF-1α degradation induce heart failure and premature death (*37*, *49*–*51*). We therefore investigated the long-term consequences of this signaling in aged MCJ^{KO} mice. At 94 weeks of age, MCJ^{KO} mice maintained superior RV function, and survival did not differ from WT animals, excluding an unfavorable effect of sustained elevated ROS or HIF-1α expression (fig. S13, D and E).

In conclusion, MCJ deficiency leads to a ROS increase, triggering the activation of the mTOR/HIF-1α axis. This sequence of events establishes a baseline pseudo-hypoxic state, improving adaptability to hypoxic challenges and providing protection against hypoxia-induced PH. The critical role of HIF-1α is evident, as inhibiting it effectively reverses this protective phenotype. These findings offer valuable insights into potential therapeutic strategies for addressing cardiovascular complications associated with chronic hypoxia.

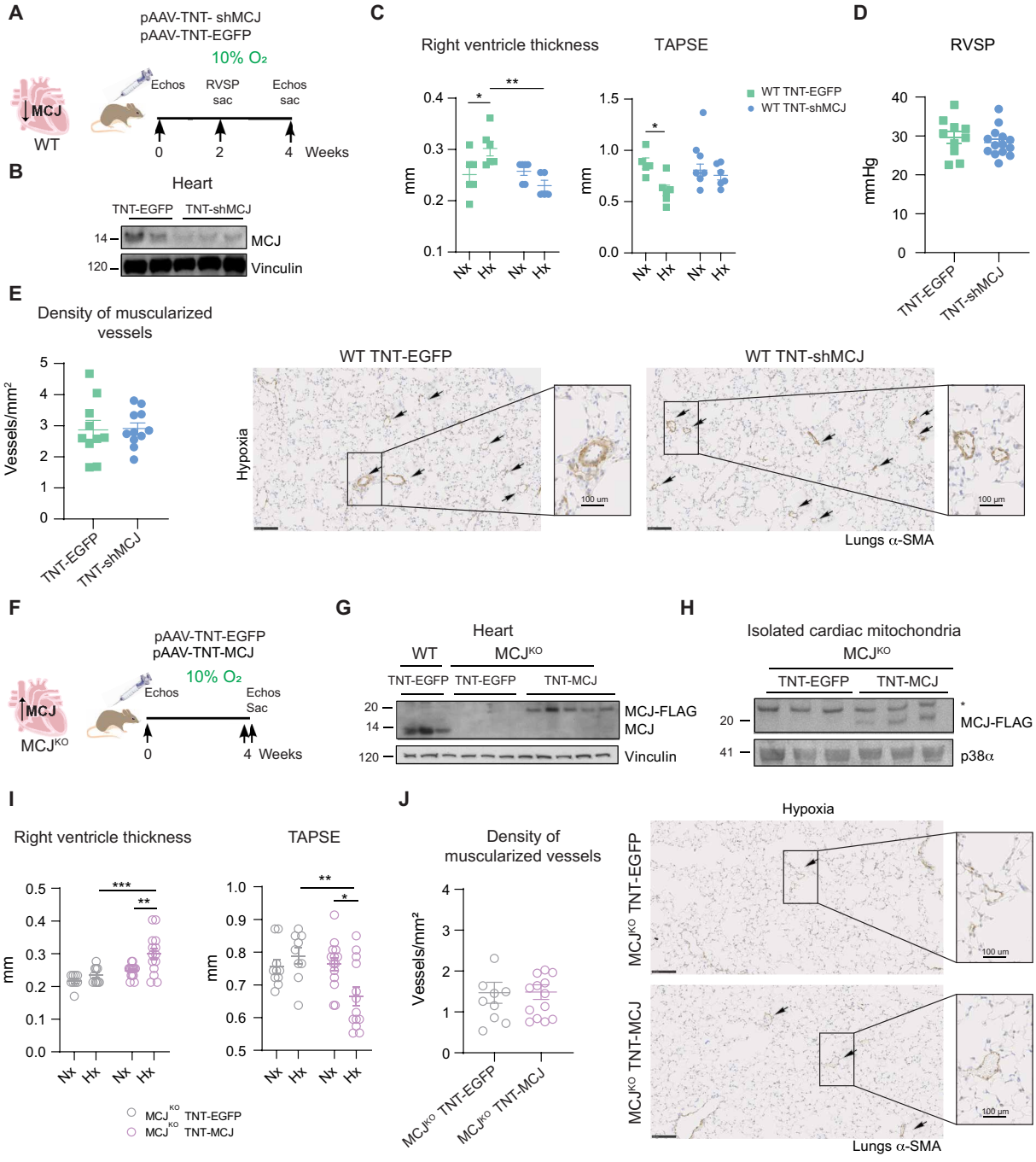

Fig. 2. Modulation of cardiac-specific MCJ expression is sufficient to determine the cardiac fate. (**A**) Experimental scheme for (B) to (E). WT mice were intravenously injected at postnatal day 1 with pAAV-TnT-shMCJ adenovirus to silence specifically MCJ expression in cardiomyocyte (WT TNT-shMCJ) or with control AAV-TNT-EGFP-Luc (WT TNT-EGFP). Adult mice were maintained in normoxia (Nx; 21% O_2) or exposed to chronic hypoxia (Hx; 10% O_2). (**B**) Immunoblot showing MCJ deletion in cardiac lysates from WT TNT-shMCJ mice. (**C**) Echocardiography of RV hypertrophy (RV thickness) and function (TAPSE) ($n = 5$ to 6, $N = 1$). (**D**) RVSP in hypoxic mice ($n = 10$ to 14, $N = 2$). (**E**) Muscularized vessel density in hypoxic lungs of mice ($n = 5$ to 10, $N = 2$). Representative immunohistochemistry of α-SMA in hypoxic lungs, amplification of remodeled vessel. Scale bars, 250 μm, 100 μm (vessel). (**F**) Experimental scheme for (G) to (J). MCJ^{KO} mice were intravenously injected at 4 weeks with pAAV-TnT-MCJ adenovirus to achieve cardiomyocyte-specific overexpression of MCJ (MCJ^{KO} TNT-MCJ) or with control AAV-TNT-EGFP-Luc (MCJ^{KO} TNT-EGFP). Adult mice were maintained in normoxia (Nx; 21% O_2) or exposed to chronic hypoxia (Hx; 10% O_2). (**G**) MCJ overexpression in cardiac lysates from MCJ^{KO} TNT-MCJ mice. (**H**) MCJ overexpression in cardiac isolated mitochondria from MCJ^{KO} TNT-MCJ mice. Nonspecific band with an asterisk. (**I**) Echocardiography of RV hypertrophy (RV thickness) and function (TAPSE) ($n = 9$ to 14, $N = 1$). (**J**) Muscularized vessel density in hypoxic lungs with a representative immunohistochemistry of α-SMA, amplification of remodeled vessels ($n = 8$ to 14, $N = 1$). Scale bars, 250 μm, 100 μm (vessel). *n*, number of biological samples; *N*, number of times that the experiment was repeated. All data are presented as means ± SEM. Statistical comparison by two-tailed Student's *t* test [(D), (E), and (J)] or two-way ANOVA with Tukey posttest [(C) and (I)]: NS, $*P < 0.05$, $**P < 0.01$, $***P < 0.001$. Panels (A) and (F) prepared using modified figures from Servier Medical Art (https://smart.servier.com/), licensed under a Creative Commons Attribution 3.0 unported license.

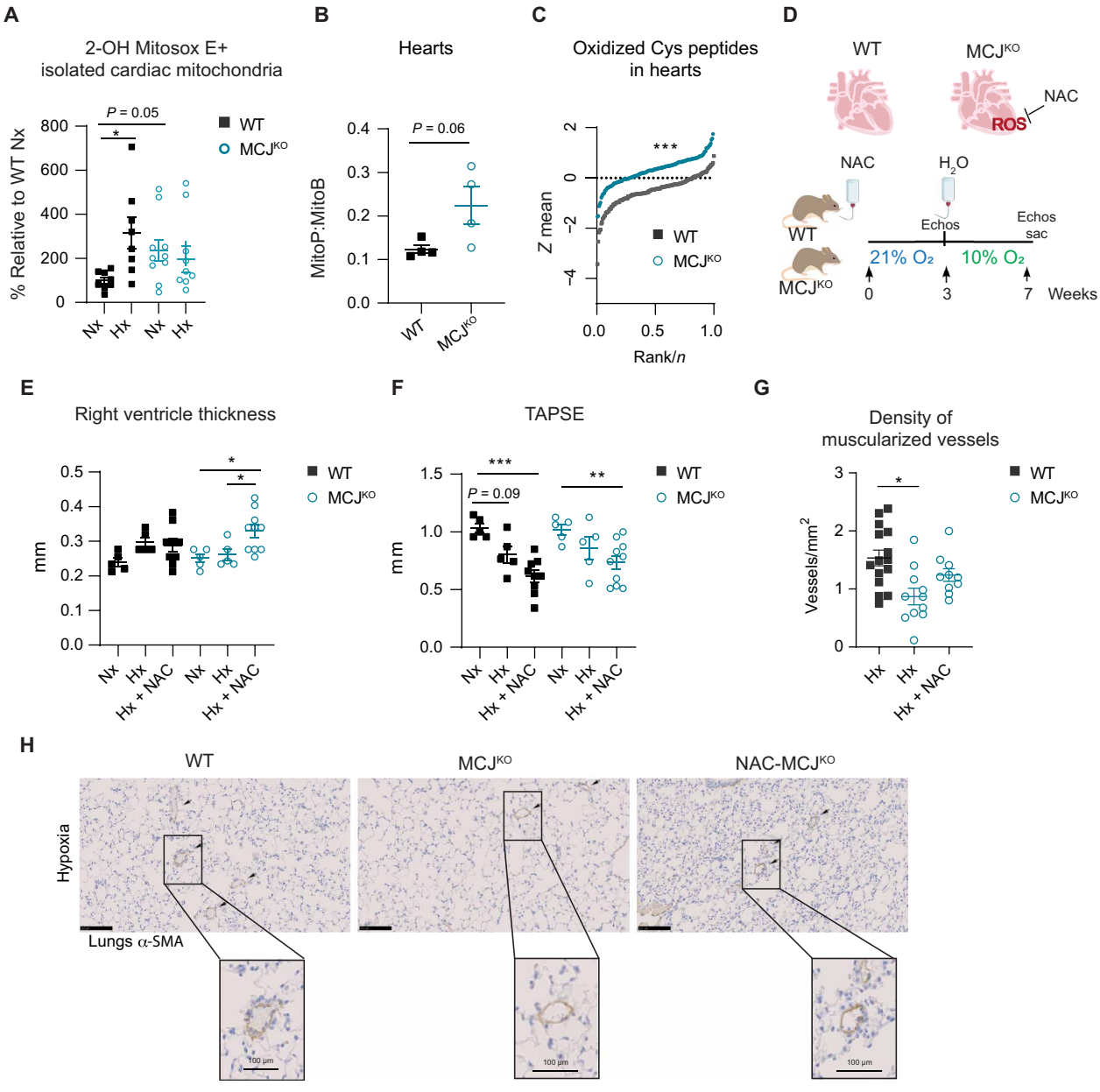

Fig. 3. Lack of MCJ leads to elevated baseline levels of ROS and impaired burst in response to hypoxia in cardiac tissue. (**A**) High-performance liquid chromatography (HPLC)–based quantification of 2-OH–mito-E+ in isolated cardiac mitochondria from normoxic (Nx; 21% O_2) or hypoxic (Hx; 7 days at 10% O_2) WT and MCJ^{KO} mice (n = 8 to 10, N = 2). (**B**) Ex vivo measurement of mitochondrial H_2O_2 with the ratiometric mass spectrometry MitoB probe which reacts with H_2O_2 forming MitoP. Mice were injected with MitoB and euthanized after 30 min (n = 4, N = 1). (**C**) Thiol redox proteomics using the FASILOX technique in cardiac tissue from normoxic (Nx; 21% O_2) WT and MCJ^{KO} mice (n = 4, N = 1). Plot showing the distributions of standardized $\log_2$-abundance ratios of oxidized Cys peptides. (**D**) Experimental protocol for (E) to (H). MCJ^{KO} mice received *N*-acetylcysteine (NAC) in drinking water for 2 weeks. After withdrawal of the treatment, they were exposed to chronic hypoxia (Hx; 10% O_2). (**E** and **F**) Echocardiography assessment of RV hypertrophy (RV thickness) and function (TAPSE) in Nx or Hx mice pretreated or not with NAC (n = 5 to 10, N = 2). (**G**) Muscularized vessel density in hypoxic lungs of WT, MCJ^{KO}, and MCJ^{KO} mice treated with NAC (n = 10 to 15, N = 2). Data for hypoxic WT and MCJ^{KO} mice from Fig. 1H were added to increase the power of the statistical test. (**H**) Representative images show α-SMA immunostaining, with amplification of a remodeled vessel in hypoxia. Scale bars, 250 µm, 100 µm (vessel). *n*, number of biological samples; *N*, number of times that the experiment was repeated. All data are presented as means ± SEM. Statistical comparison by one-way ANOVA with Dunnet's posttests compared to the control WT Nx (A), two-tailed Student's *t* test (B), Kolmogorov-Smirnov test (C), or one-way ANOVA with Tukey's posttest [(E) to (G)] [comparisons performed within the same genotype for (E) and (F)]: NS, $*P < 0.05$, $**P < 0.01$, and $***P < 0.001$. Panel (D) prepared using modified figures from Servier Medical Art (https://smart.servier.com/), licensed under a Creative Commons Attribution 3.0 unported license.

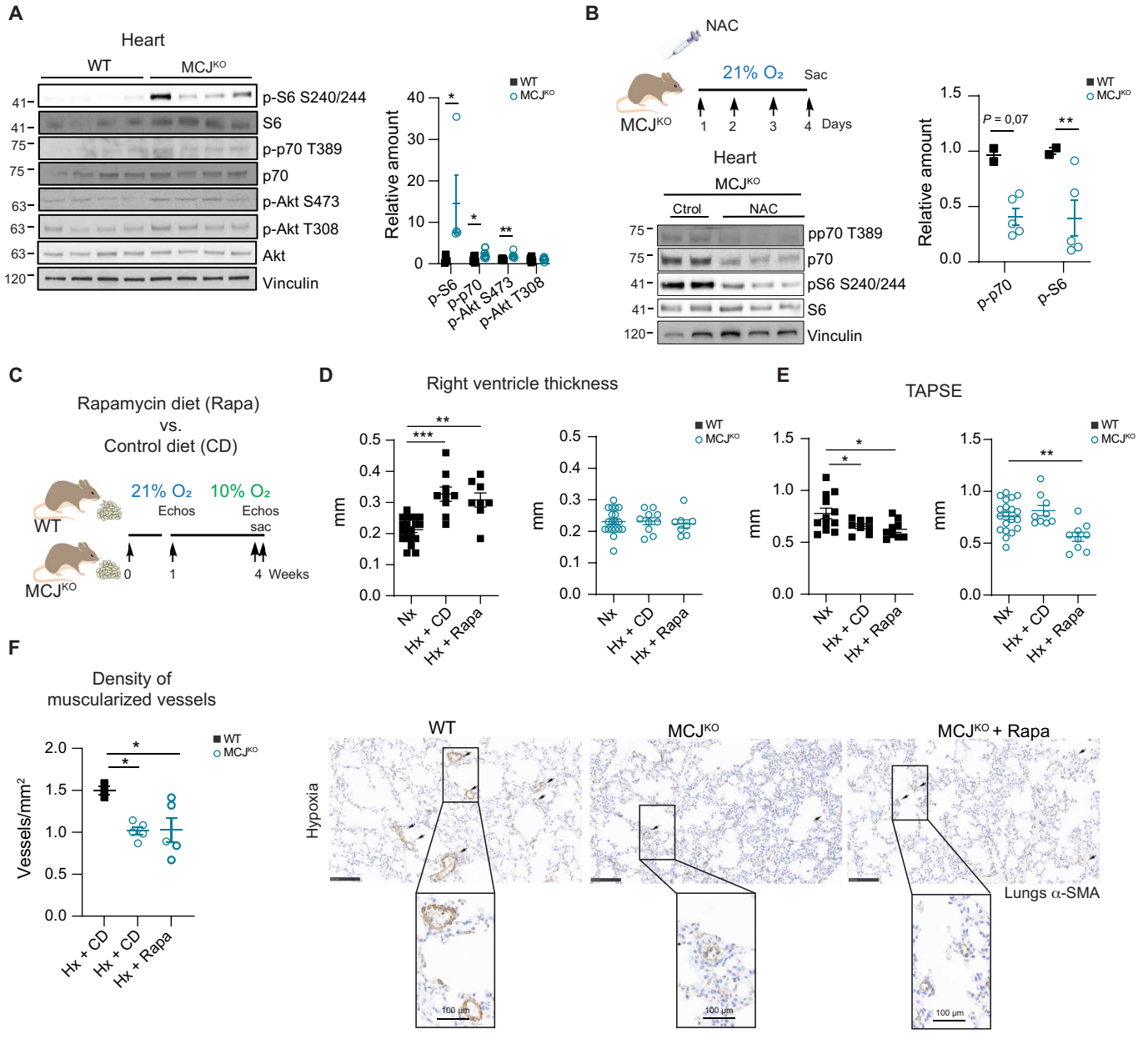

Fig. 4. MCJ^{KO} mice have higher baseline mTOR activation due to increased ROS production. (**A**) Representative immunoblots of mTOR pathway activation in heart lysates from normoxic WT and MCJ^{KO} mice ($n = 4$ to 11). (**B**) Experimental protocol to assess the effect of ROS scavenging in MCJ^{KO} mice. Mice were intraperitoneally injected during four consecutive days with the ROS scavenger NAC and euthanized at day 5. Representative immunoblots of mTOR pathway activation in normoxic MCJ^{KO} mice injected with NAC or vehicle (control) ($n = 2$ to 5). (**C**) Experimental protocol for (D) to (F). WT and MCJ^{KO} mice were fed a control diet or a diet supplemented with rapamycin (mTOR inhibitor) for 1 week and then exposed to chronic (Hx; 10% O_2). Diets were maintained until euthanasia. (**D** and **E**) Echocardiography assessment of RV hypertrophy (RV thickness) and function (TAPSE) in Nx or Hx mice fed with the control or rapamycin diet ($n = 8$ to 10, $N = 2$). (**F**) Muscularized vessel density in normoxic and hypoxic WT, MCJ^{KO}, and MCJ^{KO} lungs treated with rapamycin ($n = 3$ to 5, $N = 2$). Representative images show α-SMA immunostaining, with amplification of a remodeled vessel in hypoxia. Scale bars, 250 µm, 100 µm (vessel). *n*, number of biological samples; *N*, number of times that the experiment was repeated. All data are presented as means ± SEM. Statistical comparison by two-tailed Student's *t* test [(A) and (C)] or one-way ANOVA with Tukey's posttest [(E) to (G)]; NS, $^*P < 0.05$, $^{**}P < 0.01$, and $^{***}P < 0.001$. Panels (B) and (C) prepared using modified figures from Servier Medical Art (https://smart.servier.com/), licensed under a Creative Commons Attribution 3.0 unported license.

DISCUSSION

PH stands as a compelling clinical challenge, with detrimental effects on both the pulmonary vascular tree and the heart. The pressing need to address the cardiovascular consequences of this disease underscores the urgency of developing innovative therapeutic strategies. Understanding and modulating the response to hypoxia in this context has become a crucial focus, as oxygen deprivation not only leads to acute events, like stroke and infarction, but also contributes to the progression of chronic diseases.

In this study, we discovered that the absence of MCJ leads to preservation of cardiac function and a decrease in pulmonary remodeling under conditions of chronic hypoxia, implying a robust defense against

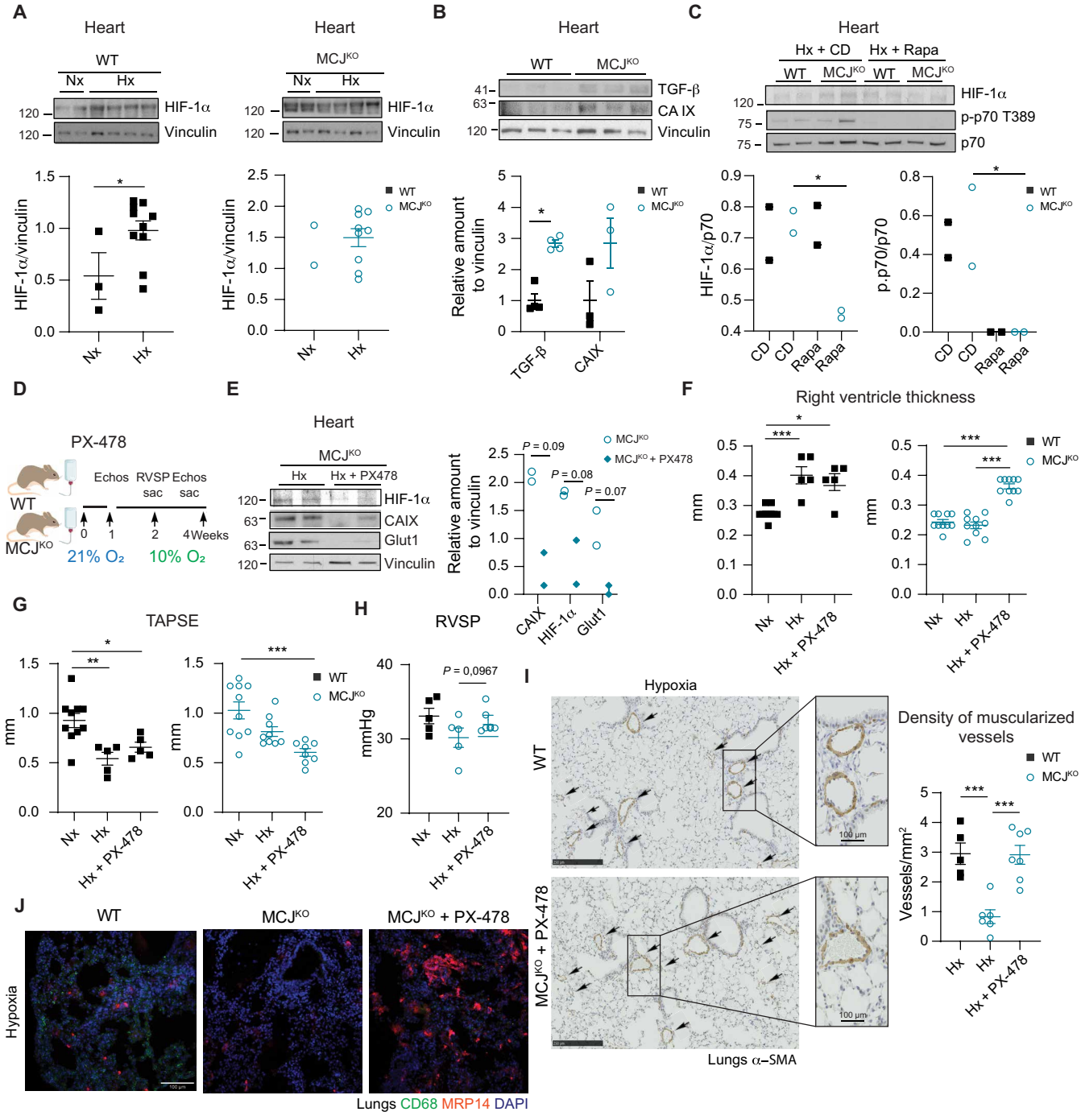

Fig. 5. MCJ^{KO} mice presented elevated HIF-1α levels, and its inhibition leads to the development of PH. (**A**) Representative immunoblot analysis of HIF-1α levels in cardiac lysates from mice maintained in normoxia (Nx; 21% O_2) or exposed to chronic hypoxia (Hx; 28 days at 10% O_2). WT and MCJ^{KO} samples were loaded and ran in the same gel ($n = 2$ to 10). (**B**) Representative immunoblot of HIF-1α downstream targets: transforming growth factor–β (TGF-β) and carbonic anhydrase IX (CA IX) in cardiac lysates from normoxic mice ($n = 3$ to 4). (**C**) mTOR pathway activation and HIF-1α expression in hypoxic WT and MCJ^{KO} mice fed with control or rapamycin diet. (**D**) Experimental protocol for (E) to (J). WT and MCJ^{KO} mice received the HIF-1 α inhibitor PX-478 in drinking water for 1 week and were then exposed to hypoxia (10% O_2) for 15 or 28 days. PX-478 treatment was maintained until euthanasia. (**E**) Immunoblots shows PX-478 efficiency in hypoxic MCJ^{KO} mice. (**F** and **G**) Echocardiography of RV hypertrophy (RV thickness) and function (TAPSE) in mice maintained in Nx or exposed to Hx with or without PX-478 treatment ($n = 5$ to 10, $N = 2$). (**H**) RVSP in WT and MCJ^{KO} mice exposed to hypoxia with or without PX-478 ($n = 5$ to 7, $N = 2$). (**I**) Muscularized vessel density in hypoxic lungs of WT and MCJ^{KO} mice ($n = 5$ to 7, $N = 2$). Representative images show α-SMA immunostaining in hypoxic WT and MCJ^{KO} lungs, amplification of a remodeled vessel. Scale bars, 250 µm, 100 µm (vessel). (**J**) Macrophages (CD68) and neutrophils (MRP14) infiltration in hypoxic lungs. Nuclei stained with DAPI. Scale bar, 100 µm. *n*, number of biological samples; *N*, number of times that the experiment was repeated. All data are presented as means ± SEM. Statistical comparison by one-way ANOVA with Tukey test [(F) to (I)]: NS, $*P < 0.05$, $**P < 0.01$, and $***P < 0.001$. Panel (D) prepared using modified figures from Servier Medical Art (https://smart.servier.com/), licensed under a Creative Commons Attribution 3.0 unported license.

PH. Assessment of cardiac molecular cues (HIF-1α and metabolomic profile) and systemic parameters (such as the altered hemogram) suggest that MCJ^{KO} mice seem to be in a basal pseudo-hypoxic state. In line with this, recent studies showed that chronic hypoxia induces organ-level rewiring, with glucose metabolism being mainly affected in cardiac tissue (*52*). Our metabolomic and proteomic data in normoxic MCJ^{KO} mice confirmed this observation. Although, MCJ^{KO} mice manage to maintain normal cardiac function, indicative of an adaptive phenotype. The bone marrow transplant experiment allowed us to rule out the immune cell involvement in the observed protection.

MCJ depletion might drive genetic adaptation to chronic hypoxia by increasing HIF-1α expression, thereby triggering defense mechanisms to deal with O_2 shortage and initiating cardioprotective programs (*53*). HIF-1α has been shown to be essential for preconditioning in ischemia/reperfusion models. While its activation leads to cardioprotection, HIF-1α repression, deletion, or inhibition abolished it (*44*, *54*, *55*). However, HIF-1α accumulation due to impaired degradation has been linked to the progression of PH, resulting in heart failure and premature death (*37*). Our results showed no short- or long-term functional consequences of increased cardiac HIF-1α expression. Unlike in previous studies, HIF-1α up-regulation in our system is driven by activation of the mTOR pathway, which increases the transcription and translation of HIF-1α without affecting its stability or degradation (*41*, *56*, *57*). This divergence suggests that the effects of elevated HIF-1α content depend on the specific molecular mechanism underlying its up-regulation.

Our findings have shed light on an important function of MCJ in regulating the ROS/mTOR/HIF-1α signaling axis. We proposed that this signaling cascade plays a pivotal role in MCJ^{KO} mice protection against hypoxia. Our study used various inhibitors (NAC, rapamycin, and PX-478) to effectively demonstrate the involvement of the ROS/mTOR and HIF-1α signaling axis in the protection conferred against hypoxia in MCJ^{KO} mice.

ROS were historically known for causing extensive oxidative damage, being implicated in aging and in the pathogenesis of several human diseases. Nowadays, it is clear that, depending on the specific threshold levels, their production site, and the cell context, they might have a homeostatic role due to their signaling capacity (*58*, *59*). In our model, the absence of MCJ results in elevated ROS levels that do not further increase under hypoxia, indicating a potential association between the oxidative burst and the pathogenesis of PH. This concept gained further support from the results of NAC treatment. Our results revealed that ROS functioned as signaling molecules, triggering the mTOR pathway, a phenomenon that has been observed in diverse contexts (*60*–*62*). Despite the observed cardiac reversal in the RV thickness and tricuspid annular plane systolic excursion (TAPSE) upon the NAC treatment, the pulmonary vascular remodeling shows no change. These results seem to indicate that modulation of ROS levels have the potential to determine the cardiac fate in an independent manner of their role in the pulmonary remodeling. These data strengthen our findings indicating that modulation of ROS, in this case by regulation of MCJ expression, allows separating the cardiac from the pulmonary outcomes in hypoxia-induced PH.

While MCJ^{KO} mice were resistant to develop PH, PX-478 resulted in PH similar to that in WT mice. Besides, rapamycin or NAC treatments only resulted in partial effects, probably due to the wide range of homeostatic signaling and cellular functions that both ROS and mTOR have. These findings highlight the importance of HIF-1α as the mediator of preserved cardiac function in the MCJ^{KO}. This "preconditioning effect" aligns with epidemiological studies showing lower mortality rates for coronary heart disease and stroke among human populations living at high altitudes (*63*, *64*). In addition, it is consistent with the capacity of chronic hypoxia to enhance myocardial tolerance to ischemia and subsequent episodes of acute severe hypoxia (*65*, *66*).

Last, our study shows that specifically targeting MCJ in cardiomyocytes could potentially be a tool against hypoxia-induced RV systolic dysfunction despite the associated pulmonary vascular remodeling (Fig. 6). Furthermore, whereas current therapies for PH rely on vasodilators, our findings provide a candidate target against PH to rescue the cardiac consequences of hypoxia exposure.

MATERIALS AND METHODS

Experimental design

Human COPD samples

Human lung tissue samples were obtained from lung transplant recipients with COPD and with or without PH (*67*). Control samples were obtained from donors undergoing surgical lung resection for lung cancer as part of a study of histology in smokers (*68*). Studies were approved by the Ethics Committee of Hospital Clinic, Barcelona, Spain, and all patients provided a written informed consent.

Lung tissue samples were collected prospectively and processed after surgery. Briefly, immediately after resection, fresh 3- to 4-mm-thick lung tissue slices were washed three times (10 min each) in cold phosphate-buffered saline (PBS) to distend collapsed areas of parenchyma and clean off embedded blood. Paraffin-embedded lung tissue blocks were cut into 5-μm sections and processed for immunohistochemistry.

Pig model of chronic RV pressure overload

Chronic RV pressure overload was modeled in castrated male Yucatan pigs. The study was approved by the Institutional Animal Research Committee and carried out in compliance with the *Guide for the Care and Use of Laboratory Animals*. Before the procedure, animals were anesthetized by intramuscular injection of ketamine (20 mg/kg), xylazine (2 mg/kg), and midazolam (0.5 mg/kg), with buprenorphine (0.3 mg/kg) for analgesia, and the animals were intubated. Briefly, four animals weighing 10 to 15 kg (between 3 and 4 months old) underwent surgical restrictive banding of the main PA using a fabric tape tailored at two-thirds of the vessel perimeter and secured with a 2-0 silk suture via a small left thoracotomy. For control experiments, a sham procedure was performed in four animals via left thoracotomy to expose and dissect the PA but omitting banding. Animals were assessed at 1, 5, and 8 months after surgery by right heart catheterization and cardiac magnetic resonance to confirm RV pressure overload and secondary cardiac adaptation (Table 1) (*69*, *70*). At the completion of the study (after surgery month 8), animals were euthanized by lethal injection of sodium pentobarbital, and hearts were excised for further studies.

Mice

Experiments were performed in WT and MCJ^{KO} (*15*) adult male mice of 8 to 14 weeks old on the C57BL/6J background. For chronic hypoxia experiments, control mice were left in normoxia (21% O_2), whereas hypoxia-treated mice were located in hypoxic chambers at 10% O_2. Analyzing the RVSP and the cardiac phenotype at the same time is unfeasible, so a time point study of the RVSP and echocardiography parameters were performed to optimize the hypoxia protocols. RVSP is normally studied at 15 days of hypoxia exposure (28 days being the time point where it reaches a plateau), while echocardiography

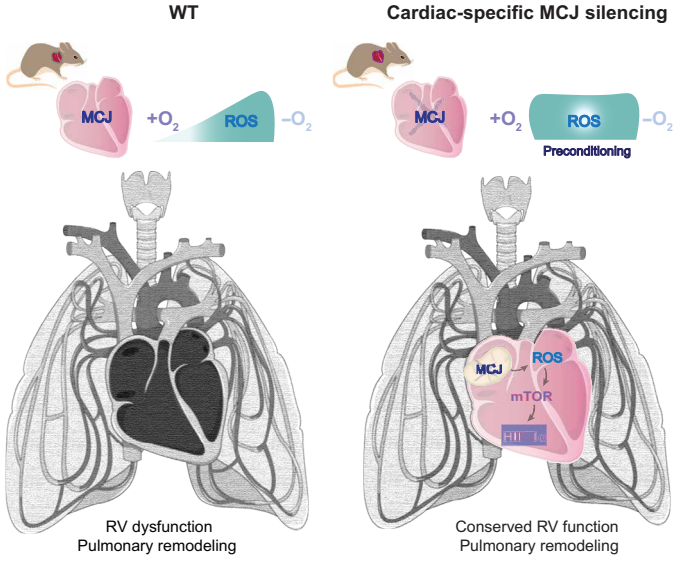

Fig. 6. Cardiac-specific modulation of MCJ is enough to rescue the cardiac function in mice with substantial lung remodeling. Lack of MCJ results in cardiac activation of the ROS/mTOR/HIF-1α pathway acting as a preconditioning for posterior hypoxic insults preventing the development of PH. In addition, specific silencing of MCJ in cardiomyocytes is enough to protect from RV dysfunction. Figure prepared using modified figures from Servier Medical Art (https://smart.servier.com/), licensed under a Creative Commons Attribution 3.0 unported license.

measurements shown alteration in both the RV thickness and diameter, with a reduction in the function only at 28 days. Thus, all experiments were performed after 28 days of hypoxic exposure except for RVSP measurements, which were performed after 15 days. Metabolomic, MitoB/P detection and mitoSOX-HPLC analysis were performed in cardiac tissue after 7 days of hypoxic exposure.

NAC administration NAC (Sigma-Aldrich, A9165) was intraperitoneally injected (500 mg/kg) to normoxic MCJ^{KO} mice for four consecutive days and euthanized at day 5. To study the effects of ROS in the cardiovascular outcome after the hypoxic treatment, MCJ^{KO} mice received a daily dose of NAC (500 mg/kg) in drinking water for 2 weeks, and, after withdrawal of the treatment, they were exposed to the chronic hypoxia protocol.

Rapamycin administration For hypoxia experiments including rapamycin administration, WT and MCJ^{KO} mice were fed a standard chow control diet [Mod LabDiet 5LG6 with 421–parts per million (PPM) Eudragit] or a chow diet with encapsulated rapamycin. The diet was begun 1 week before the hypoxia treatment and was maintained throughout the experiment. Two independent experiments were performed, each with $n = 5$ mice per group.

PX-478 2HCl administration For experiments with the HIF-1α inhibitor PX-478 2HCl (Tianpharm, China), the drug was administered at 30 mg/kg in drinking water. To achieve HIF-1α inhibition before the beginning of the experiment, administration started 1 week before the start of hypoxia exposure and was maintained throughout the experiment until euthanasia.

MitoB administration For MitoB experiments, retro-orbital injections of 75 nmol of MitoB per mouse were performed. After 30 min, mice were euthanized, and cardiac tissue were harvested, flash-frozen in liquid nitrogen, and stored at −80°C until samples were ready for processing.

Cardiac-specific deletion of MCJ To achieve cardiac-specific deletion of MCJ, WT mice at postnatal day 1 received an intravenous injection of 2×10^{11} viral particles of pAAV[miR30]-cTnT>EGFP:{mDnajc15[shRNA]}:WPRE, against the target sequence CAAGCGAGAGGCTAGTCTTATTTAGTGAAGCCACAGATG-TAAATAAGACTAGCCTCTCGCTTA.

Cardiac-specific overexpression of MCJ To achieve cardiac-specific overexpression of MCJ, 4-week MCJ^{KO} mice were intravenously injected with 2×10^{11} viral particles with p-AAV-cTNT-mDnajc15-Flag-mCherry. For both MCJ deletion and overexpression experiments, control mice were injected with virus encoding TNT-GFP luciferase.

Bone marrow transplant For the generation of chimeric mice, recipient mice carrying the differential Ptprca pan leukocyte marker (CD45.1) were irradiated with two doses of ionizing radiation (625 Gray) and then reconstitute the bone marrow using 5×10^6 donor

Table 1. Estimated median values for RV systolic pressure and RV hypertrophy for Yucatan pigs subjected to sham or PA banding surgery (interquartile range).

	RV systolic pressure (mm Hg)	RV hypertrophy (g/m^2)
Sham	31.5 (9)	14 (5)
PA banding	54.5 (9)	19.9 (3)

cells from WT or MCJ-KO mice. Mice were treated with an antibiotic cocktail containing neomycin (0.15 mg/ml; Sigma-Aldrich, catalog no. N1876-25G), kanamycin (0.15 mg/ml; Sigma-Aldrich, catalog no. K4000-5G), and gentamycin (2 mg/liter; Invitrogen, catalog no. 157110-049) in drinking water during the first 4 weeks after irradiation and waited other 4 weeks for complete bone marrow reconstitution prior experiment.

Sugen 5416 administration Semaxinib/Sugen (SU5416; MedChem Express, no. HY-10374) was prepared fresh at 5 mg/ml in the following vehicle: 0.5% (w/v) carboxyl methylcellulose sodium (Sigma-Aldrich, C5678; 500 g, low viscosity), 0.4% (v/v) polysorbate 80 (Tween 80; Sigma-Aldrich, 59924; 100 gf), and 0.9% (v/v) benzyl alcohol (Sigma-Aldrich, 402834; 100 ml). Stir the vehicle components on a warming plate until there is a clear viscous solution and then add the Sugen and sonicate in waterbath for 15 min. Three subcutaneous injections (20 mg/kg each) were administered in total to each animal: the first one before the mice entered the hypoxic chamber, and the second and third injections were given during the first and second weeks of hypoxia exposure. Mice were euthanized after 4 weeks of hypoxia.

RV hypertrophy was assessed by sectioning the heart into RV and LV + septum, and the Fulton index was estimated as RV/ (LV + septum). In all cases, echocardiography was performed before and after the hypoxia exposure, and mice were euthanized by cervical dislocation. The survival experiment was performed according to the ethical permits, echocardiography was performed at 94 weeks, and mice were monitored daily for signs of moribundity and mortality.

All mice were housed under pathogen-free conditions in the animal care facility at the Centro Nacional de Investigaciones Cardiovasculares (CNIC). Sample size was determined using the replacement, reduction and refinement (3R) rule to ensure statistical validity and significance, diseased or harmed animals were excluded, cages were randomly allocated in our animal facility, and animals were randomly assigned to different treatment groups. Animals were killed by cervical dislocation. All animal procedures were approved by the Animal Care and Use Committee at CNIC conformed to EU Directive 86/609/EEC and Recommendation 2007/526/EC regarding the protection of animals used for experimental and other scientific purposes, enacted under Spanish law 1201/2005. The protocol code is PROEX 215/18.

Hemodynamic measurements

For the measurement of RVSP, mice were anesthetized with medetomidine (1 mg/kg) and ketamine (75 mg/kg). RVSP was measured by closed-chest insertion of a Venofix A catheter (27 gauge) coupled to a pressure transducer (Transpac IV) directly into the right ventricle (RV). Hemodynamic data were recorded with a Biopac MP36R System linked to Biopac Aqcknowledge 4.1.0 software. For each mouse, mean RVSP was obtained from at least 30 s of continuous and stable heartbeat cycles without noise.

Immunoblot

Tissue or mitochondrial extracts were prepared in Triton lysis buffer: 20 mM tris (pH 7.4), 1% Triton X-100, 10% glycerol, 137 mM NaCl, 2 mM EDTA, 25 mM β-glycerophosphate, 1 mM sodium orthovanadate, 1 mM phenylmethylsulfonyl fluoride, and aprotinin and leupeptin (10 μg/ml). Extracts (12 to 20 μg of protein) were examined by SDS–polyacrylamide gel electrophoresis. Antibodies against the following targets were obtained as indicated: vinculin (Sigma-Aldrich, no. V9131, RRID:AB_477629), β-actin (Santa Cruz Biotechnology, no. sc-47778, RRID:AB_626632), glyceraldehyde-3-phosphate dehydrogenase (Santa Cruz Biotechnology, no. sc-25778, RRID:AB_10167668), HIF-1α C-Term (1:200 to 1:300; Cayman Chemical Company, no. 10006421, RRID:AB_409037), carbonic anhydrase IX/CA9 (1:1000; Novus Biologicals, no. NB100-417, RRID:AB_10003398), and Glut1 (1:500; MilliporeSigma, no. 07-1401, RRID:AB_1587074). Antibodies against the following targets were obtained from Cell Signaling Technologies: phospho-Akt S473 (no. 9271, RRID:AB_329825), phospho-Akt T308 (no. 2965S, RRID:AB_2255933), Akt (no. 9272S, RRID:AB_329827), TGF-β (no. 3711S, RRID:AB_2063354), phospho-p70S6 kinase Thr^{389} (no. 9234S, RRID:AB_2269803), p70S6 kinase (no. 9202S, RRID:AB_331676), phospho-S6 ribosomal protein $Ser^{240/244}$ (no. 5364 s, RRID:AB_10694233), and S6 ribosomal protein (no. 2217S, RRID:AB_10694233). The anti-mouse MCJ rabbit polyclonal antibody was as previously described (*15*). All antibodies were used at 1:1000 dilution unless otherwise specified. After washes, membranes were incubated with an appropriate horseradish peroxidase (HRP)–conjugated secondary antibody (GE Healthcare), and signals were detected using an enhanced chemiluminescent substrate (GE Healthcare, RPN2109).

Mouse echocardiography

Transthoracic echocardiography was performed by a blinded expert operator using a high-frequency ultrasound system (Vevo 2100, Visualsonics Inc., Canada) with a 30-MHz linear probe. Two-dimensional (2D) and M-mode (MM) echography were performed at a frame rate above 230 frames/s, and pulse-wave Doppler was acquired with a pulse repetition frequency of 40 kHz. Mice were lightly anesthetized with 0.5 to 2% isoflurane in 100% oxygen, with the isoflurane delivery adjusted to maintain the heart rate at 450 ± 50 beats per minute (bpm) and a positive podal reflex. Mice were placed in a supine position on a heated platform, and normothermia was maintained with a heat lamp and warmed ultrasound gel. Mice were continuously monitored with a base apex electrocardiogram. RV systolic function was estimated indirectly from the TAPSE, estimated from maximum lateral tricuspid annulus movement obtained from a MM four-chamber apical view. RV thickness was assessed from a rotated short axis view optimized to visualize the free RV wall. Short-axis, long-axis, B-mode, and 2D MM views were obtained as described (*71*). These images were used to calculate the LV wall thickness (as an average of the interventricular septum and the left ventricular posterior wall thicknesses) and the left ventricular volume. Cardiac function was estimated from ejection fraction (EF) values that were obtained from MM views by a blinded echocardiography expert. For EF measurements, a long- or short-axis view of the heart was selected to obtain an MM registration in a line perpendicular to the left ventricular septum and the posterior wall at the level of the mitral chordae tendineae. The isovolumetric relaxation time was measured as an indicator of diastolic dysfunction. Images were transferred to a computer and were analyzed offline with the Vevo 2100 Workstation software.

Immunostaining

Human lung sections were stained with anti-MCJ antibody (EPR12823) (1:50; Abcam, no. ab179820) followed by a biotinylated goat anti-rabbit secondary antibody (1:500; Jackson ImmunoResearch Laboratories), streptavidin-conjugated avidin–biotin complex (ABC), and 3,3′-diaminobenzidene conjugated to HRP (Vector Laboratories, catalog no. PK-6100). Immunostained sections were briefly counterstained with Nuclear Fast Red hematoxylin (Sigma-Aldrich).

The left lung lobule was inflated with 4% paraformaldehyde (PFA) and then further fixed in 4% PFA overnight at 4°C. For inflammation analysis, frozen mouse lungs were stained with rat anti-mouse CD68 purified monoclonal antibody (clone FA-11; 1:100; Bio-Rad, no. MCA1957GA, RRID:AB_324217), anti-S100A9 antibody (MRP14)

(2B10) (1/100; Abcam, no. ab105472, RRID:AB_10862594), and 4′,6-diamidino-2-phenylindole (DAPI) (Invitrogen).

Lung vasculature remodeling was assessed in paraffin-embedded sections by staining with monoclonal HRP-conjugated anti–α–smooth muscle actin (SMA) (mouse IgG2a isotype) (1:1000; Sigma-Aldrich, no. SAB4200679), which, for commercial reasons, was replaced with rabbit monoclonal (SP171) anti–α-SMA antibody (1:200; Abcam, no. ab150301) together with EnVision anti-rabbit HRP (Agilent, no. K4003, RRID:AB_2630375). Pulmonary vascular remodeling was assessed using Fiji software to quantify the density (frequency/lung area) of fully muscularized vessels (SMA^+ and with diameter of <50 μm).

RV and LV cardiomyocyte cross-sectional areas were estimated by wheat germ agglutinin (WGA) immunofluorescence, and 8-μm heart sections were prepared, washed in PBS, incubated for 2 hours in WGA–Alexa Fluor 488 lectin (no. W11261, Invitrogen, Carlsbad, California), washed, and mounted in anti-fade reagent. Four images (20×) were taken from each heart, and the diameters and areas of 100 to 200 cross-sectionally oriented myocytes were measured and analyzed with ImageJ.

Assessment of vascular function by wire myography

Vascular function was assessed as previously reported (*72*–*74*). Briefly, animals were euthanized, and lungs were excised, washed, and preserved in Krebs-Henseleit solution (KHS) (115 mM NaCl, 2.5 mM $CaCl_2$, 4.6 mM KCl, 1.2 mM KH_2PO_4, 1.2 mM $MgSO_4$, 25 mM $NaHCO_3$, 11.1 mM glucose, and 0.01 mM EDTA). PAs were gently cleaned of surrounding tissue and cut into ~2-mm-long segments. Artery rings were then mounted on two tungsten wires (25-μm diameter) in a wire myograph system (620M, Danish Myo Technology A/S, Hinnerup, Denmark) and immersed in KHS at 37°C with constant gassing (95% O_2 and 5% CO_2). Optimal vessel distension was determined by normalization using the Laplace equation [tension = (pressure × radius)/thickness] to calculate the position at which the tension was equivalent to an intraluminal pressure of 25 mmHg (L100) reported (*72*–*74*); vessels were then set to the optimal tension (physiological distension = 0.9 of L100).

After equilibration for 30 min, vasoconstriction was evaluated by exposing the rings first to 80 mM KCl and then to 1 μM phenylephrine. Consecutive treatments were separated by extensive washes and a stabilization period of at least 30 min.

The effects of acute hypoxia on the PAs were studied under resting conditions. To induce hypoxia, the organ chambers were wrapped in cling film, and the gas mixture aerating the organ bath was switched from 95% O_2, 5% CO_2 to 95% N_2, 5% CO_2. This approach generally achieved 2 to 3% oxygen saturation (Multiparametric EDGE, HI2040-02, Hanna Instruments).

qPCR assessment of inflammation markers

RNA (1 μg) was transcribed to complementary DNA (Applied Biosystems, no. 4368814), and reverse transcription quantitative polymerase chain reaction (qPCR) was performed using Fast SYBR Green probe (Applied Biosystems, no. 4385616) and appropriate primers in a 7900 Fast Real Time thermocycler (Applied Biosystems). Primers are targeted against mouse sequences (Table 2).

Isolation of lung-infiltrating leukocytes

Mice were perfused with 20 ml of PBS, and the lungs were collected. The tissue was dissociated and incubated for 30 min at 37°C with 1 ml of digestion medium [Liberase TL of 1 U/ml (Sigma-Aldrich) and deoxyribonuclease I of 1.2 U/ml (Sigma-Aldrich) in Hanks' balanced salt solution]. Cell suspension was passed through a 40-μm strainer, and the remaining tissue was washed with a syringe plunger adding 1× PBS + 2.5 mM EDTA. Samples were centrifuged at 1500 rpm for 5 min, and the pellet was resuspended in RBC lysis buffer. The reaction was stopped with PEB buffer (1× PBS + 2 mM EDTA + 1% fetal bovine serum). Samples were centrifuged at 1500 rpm for 5 min, and pellets were resuspended in PEB buffer. Leukocyte fraction was collected and stained with anti-CD45 V450 (clone 30-F11, Invitrogen), siglecF AF647 (clone E50-2440, BD Pharmingen), anti-CD11c phycoerythrin (PE)/cyanine 7 (CY7) (clone N418, BioLegend), anti-CD11b BV785 (clone M1/70, BioLegend, RRID:AB_396679), anti-Ly6G PE (clone 1A8, BD Pharmingen), anti-Ly6C BV510 (clone HK1.4, BioLegend), anti-CD64 BV605 (clone X54-5/7.1, BioLegend), and anti-CD206 *BV711* (clone C068C2, BioLegend). Cells were selected on the basis of size and complexity, single cells, and viability ($DAPI^-$, Sigma-Aldrich). Flow cytometry experiments were performed with a BD LSRFortessa (BD) equipment, and data were analyzed with FlowJo software.

Quantification of mitochondrial superoxide formation in isolated mitochondria: mitoSOX + HPLC

Mitochondrial oxidative stress and superoxide was also measured by an HPLC-based method to quantify triphenylphosphonium-linked 2-hydroxyethidium (2-OH–mito-E+) levels as previously described (*75*) and modified from another report (*76*). Briefly, the hearts from normoxic (21% O_2) and hypoxic mice (10% O_2, 1 week) were homogenized in Hepes buffer (50 mM Hepes, 70 mM sucrose, 220 mM mannitol, 1 mM EGTA, and 0.033 mM bovine serum albumin) and centrifuged at 1500*g* (10 min at 4°C) and 2000*g* for 5 min (the pellets were discarded). The supernatant was then centrifuged at 20,000*g* for 20 min, and the pellet was resuspended in 1 ml of Hepes buffer. The latter step was repeated, and the pellet was resuspended in 1 ml of tris buffer (10 mM tris, 340 mM sucrose, 100 mM KCl, and 1 mM EDTA) and kept on ice. Mitochondrial suspensions were diluted to a final protein concentration of 0.1 mg/ml in 0.5 ml of PBS buffer containing mitoSOX (5 μM) and incubated for 15 min at 37°C. After the incubation step, water:acetonitrile (1:1) was added to destroy the mitochondrial membrane and extract the mitoSOX oxidation products, samples were centrifuged, and 100 μl of the supernatant was subjected to HPLC analysis.

The system consisted of a control unit, two pumps, mixer, detectors, column oven, degasser, and an autosampler (AS-2057 plus with 4°C cooling device) from Jasco (Groß-Umstadt, Germany) and a C18-Nucleosil 100-3 (125 × 4) column from Macherey & Nagel (Düren, Germany). A high-pressure gradient was used with acetonitrile and 50 mM citrate buffer (pH 2.2) as mobile phases with the following percentages of the organic solvent: 0 min, 24%; 9 to 10 min, 24 to 53%; 10 to 25.5 min, 53 to 72%; 25.5 to 26 min, 72 to 95%; 26 to 30 min, 95%; 30 to 31 min, 95 to 24%; and 31 to 40 min, 24%. The flow was 0.55 ml/min, and mitoSOX was detected by its absorption at 360 nm, whereas 2-OH–mito-E+ and mito-E+ were detected by fluorescence (excitation at 500 nm/emission at 580 nm). The 2-OH–mito-E+ and mito-E+ standards were synthesized by the Fremy's salt and chloranil method as described (*77*). To suppress mitochondrial ROS formation, especially superoxide, selected samples were coincubated with the cell-permeable superoxide dismutase mimetic and peroxynitrite scavenger manganese(III) tetrakis (4-benzoic acid)porphyrin chloride (10 μM) or the mitochondria-targeted scavenger of ROS (2-(2,2,6,6-tetramethylpiperidin-1-oxyl-4-ylamino)-2-oxoethyl) triphenylphosphonium chloride (10 μM).

Determination of MitoP and MitoB content in cardiac tissue

Metabolite isolation Tissues were flash-frozen and powderized with a mortar and pestle in a liquid nitrogen bath. Approximately 10 mg of powder was transferred into tubes and resuspended in 1 ml of ice-cold

Table 2. Primers sequence. Fw, forward; Rev, reverse.

Primers		Sequence
Il-12b	Fw	GGAAGCACGGCAGCAGAATA
	Rev	AACTTGAGGGAGAAGTAGGAATGG
IL-6	Fw	TAGTCCTTCCTACCCCAATTTCC
	Rev	TTGGTCCTTAGCCACTCCTTC
Il-1b	Fw	GCAACTGTTCCTGAACTCAACT
	Rev	ATCTTTTGGGGTCCGTCAACT
Nos2	Fw	GTTCTCAGCCCAAGAATACAAGA
	Rev	GTGGACGGGTCGATGTCAC
Tnfa	Fw	CCCTCACACTCAGATCATCTTCT
	Rev	GCTACGACGTGGGCTACAG
Il-10	Fw	GCTCTTACTGACTGGCATGAG
	Rev	CGCAGCTCTAGGAGCATGTG
Cxcl1	Fw	CTGGGATTCACCTCAAGAACATC
	Rev	CAGGGTCAAGGCAAGCCTC
Mip1a	Fw	TTCTCTGTACCATGACACTCTGC
	Rev	CGTGGAATCTTCCGGCTGTAG
Mip2	Fw	CCAACCACCAGGCTACAGG
	Rev	GCGTCACACTCAAGCTCTG
CD206	Fw	CTCTGTTCAGCTATTGGACGC
	Rev	CGGAATTTCTGGGATTCAGCT
CCl5	Fw	CCTCACCATCATCCTCACTGCA
	Rev	TCTTCTCTGGGTTGGCACACAC
CXCL10	Fw	TGCTGGGTCTGAGTGGGACT
	Rev	CCCTATGGCCCTCATTCTCAC
CCL22	Fw	ACATCCGTCACCCTCTGCC
	Rev	TGAGAAAGGCTTTAAGAACTGGG
Clec10a	Fw	GACCACCTGTAGTGATGTGGG
	Rev	GACCACCTGTAGTGATGTGGG
Il-4	Fw	GGTCTCAACCCCCAGCTAGT
	Rev	GCCGATGATCTCTCTCAAGTG
Arg1	Fw	CTCAAGCCAAAGTCCTTAGA
	Rev	AGGAGCTGTCATTAGGGACAT
Mip1a	Fw	TTCTCTGTACCATGACACTCTGC
	Rev	CGTGGAATCTTCCGGCTGTAG
Vcam	Fw	AGTTGGGGATTCGGTTGTTCT
	Rev	CCCCTCATTCCTTACCACCC
Cxcl12	Fw	GCTCTGCATCAGTGACGGTA
	Rev	ATCTGAAGGGCACAGTTTGG
Mip1b	Fw	TTCCTGCTGTTTCTCTTACAC
	Rev	CTGTCTGCCTCTTTTGGTCAG
Ccl20	Fw	CGACTGTTGCCTCTCGTACA
	Rev	GAGGAGGTTCACAGCCCTTT

liquid chromatography–mass spectrometry (LC-MS) grade isopropanol (Thermo Fisher Scientific). Samples were vortexed for 10 min at 4°C. Then, they were centrifuged at 16,000*g* for 10 min at 4°C. The supernatant was transferred to a tube and dried down in a SpeedVac to be used for LC-MS analysis. Immediately before LC-MS analysis, samples were resuspended in 100 μl of 3:3:1 MeOH:chloroform:water.

Liquid chromatography–mass spectrometry A Qexactive Plus quadrupole orbitrap mass spectrometer (Thermo Fisher Scientific) equipped with an Ion Max source and a heated-electrospray ionization (HESI II) probe coupled to a Vanquish Horizon UHPLC System (Thermo Fisher Scientific) was used to perform MitoP:MitoB LC-MS experiments. Before operation, the instrument underwent mass calibration for positive

and negative ion mode using Calmix (Thermo Fisher Scientific) every 7 days. Dried samples were resuspended in enough HPLC-grade water to have a final concentration of 1 μg of protein per milliliter of water. The resuspended polar metabolite samples (2 μl) were injected onto a Supelco Ascentis Express C18 (2.7-μm particle size, 15 cm by 2.1 mm). The column oven was held at 25°C, and the autosampler tray was held at 4°C. Buffer A contained water with 0.1% formic acid, and Buffer B contained acetonitrile with 0.1% formic acid. A linear gradient starting at 20% Buffer B to 95% Buffer B was performed over the span of 12 min. Then, over the next minute, Buffer B dropped down to 20% and remained for an additional 2 min. The mass spectrometer was operated in full-scan, positive ion mode, with the spray voltage set to 3.0 kV, the heated capillary at 300°C, and the HESI probe at 350°C. The sheath gas flow was 30 units, the auxiliary gas flow was 3 units, and the sweep gas flow was 3 unit. MS data were collected in a range of mass/charge ratio (m/z) = 200 to 500. The resolution was set at 70,000, the AGC target at 1×10^6, and the maximum injection time at 100 ms.

REDOX proteomics

Quantitative redox proteome analysis was performed following the FASILOX technique. Briefly, tissue samples were disrupted in lysis buffer [50 mM tris-HCl (pH 8.5) and 2% SDS] containing 50 mM iodoacetamide to label free thiols (reduced Cys). Later, reversibly oxidized Cys in proteins were reduced with dithiothreitol and labeled with methyl methanethiosulfonate (MMTS), and proteins were digested. The resulting peptides were quantified using multiplexed tandem mass tags (TMT) isobaric labeling. Labeled peptides were analyzed by LC-MS/MS using a C-18 reversed-phase nano-column coupled to an Orbitrap Fusion mass spectrometer (Thermo Fisher Scientific) as described (*78*). For peptide identification, spectra were analyzed with Proteome Discoverer (version 2.1.0.81, Thermo Fisher Scientific) using SEQUEST-HT. For database searching against the UniProt mouse database (September 2018; 53,780 entries), the parameters were selected as follows: trypsin digestion with two maximum missed cleavage sites; precursor and fragment mass tolerances of 2 and 0.02 Da, respectively; TMT modification at N terminus and Lys residues as fixed modifications; and oxidation at Met and carbamidomethyl and MMTS adducts at Cys as dynamic modifications. Identification of peptides was performed using the probability ratio method (*79*), and the false discovery rate was calculated using inverted databases and the refined method (*80*), with an additional filtering for precursor mass tolerance of 15 ppm (*81*). For quantitative analysis, in-house iSanXoT program allows to quantify the intensity of the reporter ions derived from the isobaric labeling of the fragmentation spectra (*81*) on basis of the weighted spectrum, peptide, and protein (WSPP) model as described (*78*, *82*, *83*). This model, which allows to quantify abundance as a logarithmic ratio, estimates an abundance value for protein $\log_2$ ratios that are expressed as standardized variables, consisting in units of SD according to their estimated variances (Zq). Relative abundances of oxidized Cys-containing peptides were expressed as standardized $\log_2$ ratios using the Zpq variable as described (*83*).

Metabolomics (LC-MS)

Metabolite isolation Following procedures were previously described in (*84*). Cardiac tissues were flash-frozen and powderized with a mortar and pestle in a liquid nitrogen bath. Approximately 10 mg of powder was transferred into tubes and resuspended in 800 μl of ice-cold LC-MS–grade 60:40 methanol:water (Thermo Fisher Scientific). Samples were vortexed for 10 min at 4°C. Then, 500 μl of ice-cold LC-MS–grade chloroform (Thermo Fisher Scientific) was added to the lysate, and samples were vortexed for an additional 10 min at 4°C. Samples were centrifuged at 16,000*g* for 10 min at 4°C, creating a polar layer on top, a nonpolar layer on the bottom, and a protein layer at the interface. The top layer was transferred to a new tube and dried down in a SpeedVac to be used for LC-MS analysis. The nonpolar layer was discarded. The protein layer was lysed in radioimmunoprecipitation assay buffer [150 mM NaCl, 50 mM tris-HCl (pH 7.5), 0.1% SDS, 1% Triton X-100 (Sigma-Aldrich), 0.5% deoxycholate (Sigma-Aldrich), and complete EDTA-free protease inhibitor (Sigma-Aldrich)]. Protein in each sample was quantified using the Pierce BCA Protein Assay Kit (Life Technologies). Protein concentrations were used for normalization of sample inputs before LC-MS analysis.

Liquid chromatography–mass spectrometry A Qexactive Plus quadrupole orbitrap mass spectrometer (Thermo Fisher Scientific) equipped with an Ion Max source and a HESI II probe coupled to a Vanquish Horizon UHPLC System (Thermo Fisher Scientific) was used to perform LC-MS experiments. Before operation, the instrument underwent mass calibration for positive and negative ion mode using Calmix (Thermo Fisher Scientific) every 7 days. Dried samples were resuspended in enough HPLC-grade water to have a final concentration of 1 μg of protein per milliliter of water. Resuspended polar metabolite samples (2 μl) were injected onto a SeQuant ZIC-pHILIC 5 μm 150 by 2.1 mm analytical column equipped with a 2.1 mm–by–20 mm guard column (MilliporeSigma). The column oven was held at 25°C, and the autosampler tray was held at 4°C. Buffer A was composed of 20 mM ammonium carbonate and 0.1% ammonium hydroxide. Buffer B was composed of 100% acetonitrile. The chromatographic gradient was run at a flow rate of 0.150 ml/min as follows: 0 to 20 min, linear gradient from 80 to 20% B; 20 to 20.5 min, linear gradient from 20 to 80% B; and 20.5 to 28 min, hold at 80% B. The mass spectrometer was operated in full-scan, polarity switching mode, with the spray voltage set to 4.0 kV, the heated capillary at 350°C, and the HESI probe at 350°C. The sheath gas flow was 10 units, the auxiliary gas flow was 2 units, and the sweep gas flow was 1 unit. MS data were collected in a range of $m/z = 70$ to 1000. The resolution was set at 70,000, the AGC target at 1×10^6, and the maximum injection time at 20 ms. Differentially encountered metabolites ($P < 0.05$) were analyzed by metabolite set enrichment analysis using MetaboAnalyst 5.0. A joint pathway analysis was performed integrating proteomics and metabolomics data using MetaboAnalyst 5.0.

Hematological analyses

The hematological profile was determined in blood samples collected with EDTA using the hematology analyzer Pentra 80 (HORIBA ABX SAS).

Statistical analysis

Between-group differences were examined for statistical significance by two-tailed Student's t test or by one-way or two-way analysis of variance (ANOVA) coupled to Tukey or Dunnet's posttest, as indicated. Pearson correlation analysis was performed to study correlation between variables. Distributions from different groups were compared by Kolmogorov-Smirnov test. Note that n refers to number of biological samples, while N is number of times that the experiment was repeated. Survival curves were analyzed by Mantel-Cox log-rank test. Error bars represent SEM.

Supplementary Materials

This PDF file includes:

Figs. S1 to S13
Tables S1 and S2
Legend for table S3

Other Supplementary Material for this manuscript includes the following:

Table S3

REFERENCES AND NOTES

1. J. Arias-Stella, M. Saldana, The terminal portion of the pulmonary arterial tree in people native to high altitudes. *Circulation* **28**, 915–925 (1963).
2. L. Zhao, Chronic hypoxia-induced pulmonary hypertension in rat: The best animal model for studying pulmonary vasoconstriction and vascular medial hypertrophy. *Drug Discov. Today Dis. Model.* **7**, 83–88 (2010).
3. S. D. Nathan, J. A. Barbera, S. P. Gaine, S. Harari, F. J. Martinez, H. Olschewski, K. M. Olsson, A. J. Peacock, J. Pepke-Zaba, S. Provencher, N. Weissmann, W. Seeger, Pulmonary hypertension in chronic lung disease and hypoxia. *Eur. Respir. J.* **53**, 1801914 (2019).
4. M. Humbert, N. W. Morrell, S. L. Archer, K. R. Stenmark, M. R. MacLean, I. M. Lang, B. W. Christman, E. K. Weir, O. Eickelberg, N. F. Voelkel, M. Rabinovitch, Cellular and molecular pathobiology of pulmonary arterial hypertension. *J. Am. Coll. Cardiol.* **43**, 13S–24S (2004).
5. M. Humbert, C. Guignabert, S. Bonnet, P. Dorfmüller, J. R. Klinger, M. R. Nicolls, A. J. Olschewski, S. S. Pullamsetti, R. T. Schermuly, K. R. Stenmark, M. Rabinovitch, Pathology and pathobiology of pulmonary hypertension: State of the art and research perspectives. *Eur. Respir. J.* **53**, 1801887 (2019).
6. M. Gredic, I. Blanco, G. Kovacs, Z. Helyes, P. Ferdinandy, H. Olschewski, J. A. Barberà, N. Weissmann, Pulmonary hypertension in chronic obstructive pulmonary disease. *Br. J. Pharmacol.* **178**, 132–151 (2021).
7. L. S. Howard, Prognostic factors in pulmonary arterial hypertension: Assessing the course of the disease. *Eur. Respir. Rev.* **20**, 236–242 (2011).
8. A. Gómez, D. Bialostozky, A. Zajarias, E. Santos, A. Palomar, M. L. Martínez, J. Sandoval, Right ventricular ischemia in patients with primary pulmonary hypertension. *J. Am. Coll. Cardiol.* **38**, 1137–1142 (2001).
9. K. Asosingh, S. Erzurum, Mechanisms of right heart disease in pulmonary hypertension (2017 Grover Conference Series). *Pulm. Circ.* **8**, 2045893217753121 (2018).
10. G. Ruiter, Y. Ying Wong, F. S. De Man, M. Louis Handoko, R. T. Jaspers, P. E. Postmus, N. Westerhof, H. W. M. Niessen, W. J. Van Der Laarse, A. Vonk-Noordegraaf, Right ventricular oxygen supply parameters are decreased in human and experimental pulmonary hypertension. *J. Heart Lung Transplant.* **32**, 231–240 (2013).
11. M. Oknińska, Z. Zambrowska, K. Zajda, A. Paterek, K. Brodaczewska, U. Mackiewicz, C. Szczylik, A. Torbicki, C. Kieda, M. Mączewski, Right ventricular myocardial oxygen tension is reduced in monocrotaline-induced pulmonary hypertension in the rat and restored by myo-inositol trispyrophosphate. *Sci. Rep.* **11**, 18002 (2021).
12. L. C. Heather, M. A. Cole, J. J. Tan, L. J. A. Ambrose, S. Pope, A. H. Abd-Jamil, E. E. Carter, M. S. Dodd, K. K. Yeoh, C. J. Schofield, K. Clarke, Metabolic adaptation to chronic hypoxia in cardiac mitochondria. *Basic Res. Cardiol.* **107**, 268 (2012).
13. D. P. Champagne, K. M. Hatle, K. A. Fortner, A. D'Alessandro, T. M. Thornton, R. Yang, D. Torralba, J. Tomás-Cortázar, Y. W. Jun, K. H. Ahn, K. C. Hansen, L. Haynes, J. Anguita, M. Rincon, Fine-tuning of $CD8^+$ T cell mitochondrial metabolism by the respiratory chain repressor MCJ dictates protection to influenza virus. *Immunity* **44**, 1299–1311 (2016).
14. L. Barbier-Torres, P. Iruzubieta, D. Fernández-Ramos, T. C. Delgado, D. Taibo, V. Guitiérrez-De-Juan, M. Varela-Rey, M. Azkargorta, N. Navasa, P. Fernández-Tussy, I. Zubiete-Franco, J. Simon, F. Lopitz-Otsoa, S. Lachiondo-Ortega, J. Crespo, S. Masson, M. V. McCain, E. Villa, H. Reeves, F. Elortza, M. I. Lucena, M. I. Hernández-Alvarez, A. Zorzano, R. J. Andrade, S. C. Lu, J. M. Mato, J. Anguita, M. Rincón, M. L. Martínez-Chantar, The mitochondrial negative regulator MCJ is a therapeutic target for acetaminophen-induced liver injury. *Nat. Commun.* **8**, 2068 (2017).
15. K. M. Hatle, P. Gummadidala, N. Navasa, E. Bernardo, J. Dodge, B. Silverstrim, K. Fortner, E. Burg, B. T. Suratt, J. Hammer, M. Radermacher, D. J. Taatjes, T. Thornton, J. Anguita, M. Rincon, MCJ/DnaJC15, an endogenous mitochondrial repressor of the respiratory chain that controls metabolic alterations. *Mol. Cell. Biol.* **33**, 2302–2314 (2013).
16. L. Barbier-Torres, K. A. Fortner, P. Iruzubieta, T. C. Delgado, E. Giddings, Y. Chen, D. Champagne, D. Fernández-Ramos, D. Mestre, B. Gomez-Santos, M. Varela-Rey, V. G. de Juan, P. Fernández-Tussy, I. Zubiete-Franco, C. García-Monzón, Á. González-Rodríguez, D. Oza, F. Valença-Pereira, Q. Fang, J. Crespo, P. Aspichueta, F. Tremblay, B. C. Christensen, J. Anguita, M. L. Martínez-Chantar, M. Rincón, Silencing hepatic MCJ attenuates non-alcoholic fatty liver disease (NAFLD) by increasing mitochondrial fatty acid oxidation. *Nat. Commun.* **11**, 3360 (2020).
17. G. Strathdee, B. R. R. Davies, J. K. K. Vass, N. Siddiqui, R. Brown, Cell type-specific methylation of an intronic CpG island controls expression of the MCJ gene. *Carcinogenesis* **25**, 693–701 (2004).
18. J. C. Lindsey, M. E. Lusher, G. Strathdee, R. Brown, R. J. Gilbertson, S. Bailey, D. W. Ellison, S. C. Clifford, Epigenetic inactivation of MCJ (DNAJD1) in malignant paediatric brain tumours. *Int. J. Cancer* **118**, 346–352 (2006).
19. V. Shridhar, V. Shridhar, K. C. Bible, K. C. Bible, J. Staub, J. Staub, R. Avula, R. Avula, Y. K. Lee, Y. K. Lee, K. Kalli, K. Kalli, H. Huang, H. Huang, L. C. Hartmann, L. C. Hartmann, S. H. Kaufmann, S. H. Kaufmann, D. I. Smith, D. I. Smith, Loss of expression of a new member of the DNAJ protein family confers resistance to chemotherapeutic agents used in the treatment of ovarian cancer. *Cancer Res.* **61**, 4258–4265 (2001).
20. N. Navasa, I. Martín, J. M. Iglesias-Pedraz, N. Beraza, E. Atondo, H. Izadi, F. Ayaz, S. Fernández-Álvarez, K. Hatle, A. Som, O. Dienz, B. A. Osborne, M. L. Martínez-Chantar, M. Rincón, J. Anguita, Regulation of oxidative stress by methylation-controlled J protein controls macrophage responses to inflammatory insults. *J. Infect. Dis.* **211**, 135–145 (2015).
21. P. Iruzubieta, N. Goikoetxea-Usandizaga, L. Barbier-Torres, M. Serrano-Maciá, D. Fernández-Ramos, P. Fernández-Tussy, V. Gutiérrez-de-Juan, S. Lachiondo-Ortega, J. Simon, M. Bravo, F. Lopitz-Otsoa, M. Robles, C. Ferre-Aracil, M. Varela-Rey, N. Elguezabal, J. L. Calleja, S. C. Lu, M. Milkiewicz, P. Milkiewicz, J. Anguita, M. J. Monte, J. J. G. Marin, M. López-Hoyos, T. C. Delgado, M. Rincón, J. Crespo, M. L. Martínez-Chantar, Boosting mitochondria activity by silencing MCJ overcomes cholestasis-induced liver injury. *JHEP Rep.* **3**, 100276 (2021).
22. B. D. Kent, P. D. Mitchell, W. T. Mcnicholas, Hypoxemia in patients with COPD: Cause, effects, and disease progression. *Int. J. Chron. Obstruct. Pulmon. Dis.* **6**, 199–208 (2011).
23. C. L. Li, M. H. Lin, P. S. Chen, Y. C. Tsai, L. S. Shen, H. C. Kuo, S. F. Liu, Using the BODE index and comorbidities to predict health utilization resources in chronic obstructive pulmonary disease. *Int. J. Chron. Obstruct. Pulmon. Dis.* **15**, 389–395 (2020).
24. P. Modi, M. Cascella, *Diffusing Capacity of the Lungs for Carbon Monoxide* (StatPearls Publishing, 2023).
25. S. Rosenkranz, L. S. Howard, M. Gomberg-Maitland, M. M. Hoeper, Systemic consequences of pulmonary hypertension and right-sided heart failure. *Circulation* **141**, 678–693 (2020).
26. K. H. Andersen, M. Iversen, J. Kjaergaard, J. Mortensen, J. E. Nielsen-Kudsk, E. Bendstrup, R. Videbaek, J. Carlsen, Prevalence, predictors, and survival in pulmonary hypertension related to end-stage chronic obstructive pulmonary disease. *J. Heart Lung Transplant.* **31**, 373–380 (2012).
27. M. K. Friedberg, A. N. Redington, Right versus left ventricular failure. *Circulation* **129**, 1033–1044 (2014).
28. T. Chen, C. Yang, M. Li, X. Tan, Alveolar hypoxia-induced pulmonary inflammation: From local initiation to secondary promotion by activated systemic inflammation. *J. Vasc. Res.* **53**, 317–329 (2016).
29. C. Madjdpour, U. R. Jewell, S. Kneller, U. Ziegler, R. Schwendener, C. Booy, L. Klausli, T. Pasch, R. C. Schimmer, B. Beck-Schimmer, Decreased alveolar oxygen induces lung inflammation. *Am. J. Physiol. Lung Cell. Mol. Physiol.* **284**, L360–L367 (2003).
30. M. Rabinovitch, W. Gamble, A. S. Nadas, O. S. Miettinen, L. Reid, Rat pulmonary circulation after chronic hypoxia: Hemodynamic and structural features. *Am. J. Physiol.* **236**, H818–H827 (1979).
31. K. R. Stenmark, J. Fasules, D. M. Hyde, N. F. Voelkel, J. Henson, A. Tucker, H. Wilson, J. T. Reeves, Severe pulmonary hypertension and arterial adventitial changes in newborn calves at 4, 300 m. *J. Appl. Physiol.* **62**, 821–830 (1987).
32. N. Sommer, A. Dietrich, R. T. Schermuly, H. A. Ghofrani, T. Gudermann, R. Schulz, W. Seeger, F. Grimminger, N. Weissmann, Regulation of hypoxic pulmonary vasoconstriction: Basic mechanisms. *Eur. Respir. J.* **32**, 1639–1651 (2008).
33. N. Sommer, I. Strielkov, O. Pak, N. Weissmann, Oxygen sensing and signal transduction in hypoxic pulmonary vasoconstriction. *Eur. Respir. J.* **47**, 288–303 (2016).
34. R. M. Leach, H. M. Hill, V. A. Snetkov, T. P. Robertson, J. P. T. Ward, Divergent roles of glycolysis and the mitochondrial electron transport chain in hypoxic pulmonary vasoconstriction of the rat: Identity of the hypoxic sensor. *J. Physiol.* **536**, 211–224 (2001).
35. C. Bueno-Beti, L. Hadri, R. J. Hajjar, Y. Sassi, The Sugen 5416/Hypoxia mouse model of pulmonary arterial hypertension. *Methods Mol. Biol.* **1816**, 243–252 (2018).
36. J. P. Dignam, T. E. Scott, B. K. Kemp-Harper, A. J. Hobbs, Animal models of pulmonary hypertension: Getting to the heart of the problem. *Br. J. Pharmacol.* **179**, 811–837 (2022).
37. M. Hölscher, K. Schäfer, S. Krull, K. Farhat, A. Hesse, M. Silter, Y. Lin, B. J. Pichler, P. Thistlethwaite, A. El-Armouche, L. S. Maier, D. M. Katschinski, A. Zieseniss, Unfavourable consequences of chronic cardiac HIF-1α stabilization. *Cardiovasc. Res.* **94**, 77–86 (2012).
38. J. Nuche, T. S. de la Cal, C. J. L. Guarch, F. López-Medrano, C. P. O. Delgado, F. A. Ynsaurriaga, J. F. Delgado, B. Ibáñez, E. Oliver, P. E. Subías, Effect of Coronavirus disease 2019 in pulmonary circulation. The particular scenario of precapillary pulmonary hypertension. *Diagnostics* **10**, 548 (2020).
39. G. G. Chiang, R. T. Abraham, Phosphorylation of Mammalian Target of Rapamycin (mTOR) at Ser-2448 IsMediated by p70S6 Kinase *. *J. Biol. Chem.* **280**, 25485–25490 (2005).
40. S. C. Land, A. R. Tee, Hypoxia-inducible factor 1alpha is regulated by the mammalian target of rapamycin (mTOR) via an mTOR signaling motif. *J. Biol. Chem.* **282**, 20534–20543 (2007).
41. K. M. Dodd, J. Yang, M. H. Shen, J. R. Sampson, A. R. Tee, mTORC1 drives HIF-1α and VEGF-A signalling via multiple mechanisms involving 4E-BP1, S6K1 and STAT3. *Oncogene* **34**, 2239–2250 (2015).
42. G. L. Semenza, HIF-1 and mechanisms of hypoxia sensing. *Curr. Opin. Cell Biol.* **13**, 167–171 (2001).
43. Z. Cai, H. Zhong, M. Bosch-Marce, K. Fox-Talbot, L. Wang, C. Wei, M. A. Trush, G. L. Semenza, Complete loss of ischaemic preconditioning-induced cardioprotection in mice with partial deficiency of HIF-1α. *Cardiovasc. Res.* **77**, 463–470 (2008).
44. T. Eckle, D. Kohler, R. Lehmann, K. C. E. Kasmi, H. K. Eltzschig, Hypoxia-inducible factor-1 is central to cardioprotection a new paradigm for ischemic preconditioning. *Circulation* **118**, 166–175 (2008).

45. M. Y. Koh, T. Spivak-Kroizman, S. Venturini, S. Welsh, R. R. Williams, D. L. Kirkpatrick, G. Powis, Molecular mechanisms for the activity of PX-478, an antitumor inhibitor of the hypoxia-inducible factor-1α. *Mol. Cancer Ther.* **7**, 90–100 (2008).
46. B. González-Terán, J. A. López, E. Rodríguez, L. Leiva, S. Martínez-Martínez, J. A. Bernal, L. J. Jiménez-Borreguero, J. M. Redondo, J. Vazquez, G. Sabio, p38γ and δ promote heart hypertrophy by targeting the mTOR-inhibitory protein DEPTOR for degradation. *Nat. Commun.* **7**, 10477 (2016).
47. R. Romero-Becerra, A. M. Santamans, C. Folgueira, G. Sabio, p38 MAPK Pathway in the heart: New insights in health and disease. *Int. J. Mol. Sci.* **21**, 7412 (2020).
48. R. Romero-Becerra, A. Mora, E. Manieri, I. Nikolic, A. M. Santamans, V. Montalvo-Romeral, F. M. Cruz, E. Rodríguez, M. León, L. Leiva-Vega, L. Sanz, V. Bondía, D. Filgueiras-Rama, L. J. Jiménez-Borreguero, J. Jalife, B. Gonzalez-Teran, G. Sabio, MKK6 deficiency promotes cardiac dysfunction through MKK3-p38γ/δ-mTOR hyperactivation. *eLife* **11**, e75250 (2022).
49. A. Mongirdienė, L. Skrodenis, L. Varoneckaitė, G. Mierkytė, J. Gerulis, Reactive oxygen species induced pathways in heart failure pathogenesis and potential therapeutic strategies. *Biomedicine* **10**, 602 (2022).
50. B. Schöttker, K. U. Saum, E. H. J. M. Jansen, P. Boffetta, A. Trichopoulou, B. Holleczek, A. K. Dieffenbach, H. Brenner, Oxidative stress markers and all-cause mortality at older age: A population-based cohort study. *J. Gerontol. A Biol. Sci. Med. Sci.* **70**, 518–524 (2015).
51. S. Dey, D. DeMazumder, A. Sidor, D. Brian Foster, B. O'Rourke, Mitochondrial ros drive sudden cardiac death and chronic proteome remodeling in heart failure. *Circ. Res.* **123**, 356–371 (2018).
52. A. D. Midha, Y. Zhou, B. B. Queliconi, A. M. Barrios, A. G. Haribowo, B. T. L. Chew, C. O. Y. Fong, J. E. Blecha, H. VanBrocklin, Y. Seo, I. H. Jain, Organ-specific fuel rewiring in acute and chronic hypoxia redistributes glucose and fatty acid metabolism. *Cell Metab.* **35**, 504–516.e5 (2023).
53. M. F. Essop, Cardiac metabolic adaptations in response to chronic hypoxia. *J. Physiol.* **584**, 715–726 (2007).
54. H. Tang, A. Babicheva, K. M. McDermott, Y. Gu, R. J. Ayon, S. Song, Z. Wang, A. Gupta, T. Zhou, X. Sun, S. Dash, Z. Wang, A. Balistrieri, Q. Zheng, A. G. Cordery, A. A. Desai, F. Rischard, Z. Khalpey, J. Wang, S. M. Black, J. G. N. Garcia, A. Makino, J. X. J. Yuan, Endothelial HIF-2α contributes to severe pulmonary hypertension due to endothelial-to-mesenchymal transition. *Am. J. Physiol. Lung Cell. Mol. Physiol.* **314**, L256–L275 (2018).
55. K. Sarkar, Z. Cai, R. Gupta, N. Parajuli, K. Fox-Talbot, M. S. Darshan, F. J. Gonzalez, G. L. Semenza, Hypoxia-inducible factor 1 transcriptional activity in endothelial cells is required for acute phase cardioprotection induced by ischemic preconditioning. *Proc. Natl. Acad. Sci. U. S. A.* **109**, 10504–10509 (2012).
56. M. A. C. Déry, M. D. Michaud, D. E. Richard, Hypoxia-inducible factor 1: Regulation by hypoxic and non-hypoxic activators. *Int. J. Biochem. Cell Biol.* **37**, 535–540 (2005).
57. D. E. Richard, E. Berra, J. Pouyssegur, Nonhypoxic pathway mediates the induction of hypoxia-inducible factor 1α in vascular smooth muscle cells. *J. Biol. Chem.* **275**, 26765–26771 (2000).
58. A. L. Santos, S. Sinha, A. B. Lindner, The Good, the Bad, and the Ugly of ROS: New insights on aging and aging-related diseases from eukaryotic and prokaryotic model organisms. *Oxid. Med. Cell. Longev.* **2018**, 1941285 (2018).
59. C. R. Reczek, N. S. Chandel, ROS-dependent signal transduction. *Curr. Opin. Cell Biol.* **33**, 8–13 (2015).
60. M. Haissaguerre, A. Ferrière, V. Simon, N. Saucisse, N. Dupuy, C. André, S. Clark, O. Guzman-Quevedo, A. Tabarin, D. Cota, mTORC1-dependent increase in oxidative metabolism in POMC neurons regulates food intake and action of leptin. *Mol. Metab.* **12**, 98–106 (2018).
61. L. Chen, B. Xu, L. Liu, Y. Luo, H. Zhou, W. Chen, T. Shen, X. Han, C. D. Kontos, S. Huang, Cadmium induction of reactive oxygen species activates the mTOR pathway, leading to neuronal cell death. *Free Radic. Biol. Med.* **50**, 624–632 (2011).
62. J. H. Kim, T. G. Choi, S. Park, H. R. Yun, N. N. Y. Nguyen, Y. H. Jo, M. Jang, J. Kim, J. Kim, I. Kang, J. Ha, M. P. Murphy, D. G. Tang, S. S. Kim, Mitochondrial ROS-derived PTEN oxidation activates PI3K pathway for mTOR-induced myogenic autophagy. *Cell Death Differ.* **25**, 1921–1937 (2018).
63. E. A. Mortimer, R. R. Monson, B. MacMahon, Reduction in mortality from coronary heart disease in men residing at high altitude. *N. Engl. J. Med.* **296**, 581–585 (1977).
64. D. Faeh, F. Gutzwiller, M. Bopp, Swiss National Cohort Study Group, Lower mortality from coronary heart disease and stroke at higher altitudes in Switzerland. *Circulation* **120**, 495–501 (2009).
65. M. Tajima, D. Katayose, M. Bessho, S. Isoyama, Acute ischaemic preconditioning and chronic hypoxia independently increase myocardial tolerance to ischaemia. *Cardiovasc. Res.* **28**, 312–319 (1994).
66. H. S. Silverman, S. K. Wei, M. C. P. Haigney, C. J. Ocampo, M. D. Stern, Myocyte adaptation to chronic hypoxia and development of tolerance to subsequent acute severe hypoxia. *Circ. Res.* **80**, 699–707 (1997).
67. V. I. Peinado, F. P. Gómez, J. A. Barberà, A. Roman, M. Angels Montero, J. Ramírez, J. Roca, R. Rodriguez-Roisin, Pulmonary vascular abnormalities in chronic obstructive pulmonary disease undergoing lung transplant. *J. Heart Lung Transplant.* **32**, 1262–1269 (2013).
68. J. García-Lucio, G. Argemi, O. Tura-Ceide, M. Diez, T. Paul, C. Bonjoch, N. Coll-Bonfill, I. Blanco, J. A. Barberá, M. M. Musri, V. I. Peinado, Gene expression profile of angiogenic factors in pulmonary arteries in COPD: Relationship with vascular remodeling. *Am. J. Physiol. Lung Cell. Mol. Physiol.* **310**, L583–L592 (2016).
69. D. Pereda, I. García-Lunar, F. Sierra, D. Sánchez-Quintana, E. Santiago, C. Ballesteros, J. F. Encalada, J. Sánchez-González, V. Fuster, B. Ibánez, A. García-Álvarez, Magnetic resonance characterization of cardiac adaptation and myocardial fibrosis in pulmonary hypertension secondary to systemic-to-pulmonary shunt. *Circ. Cardiovasc. Imaging* **9**, e004566 (2016).
70. I. Garcia-Lunar, D. Pereda, E. Santiago, N. Solanes, J. Nuche, M. Ascaso, J. Bobí, F. Sierra, A. P. Dantas, C. Galán, R. San Antonio, D. Sánchez-Quintana, J. Sánchez-González, J. A. Barberá, M. Rigol, V. Fuster, B. Ibáñez, M. Sabaté, A. García-Álvarez, Effect of pulmonary artery denervation in postcapillary pulmonary hypertension: Results of a randomized controlled translational study. *Basic Res. Cardiol.* **114**, 5 (2019).
71. A. Cruz-Adalia, L. J. Jiménez-Borreguero, M. Ramírez-Huesca, I. Chico-Calero, O. Barreiro, E. López-Conesa, M. Fresno, F. Sánchez-Madrid, P. Martín, CD69 limits the severity of cardiomyopathy after autoimmune myocarditis. *Circulation* **122**, 1396–1404 (2010).
72. L. Del Campo, A. Sánchez-López, C. González-Gómez, M. J. Andrés-Manzano, B. Dorado, V. Andrés, Vascular smooth muscle cell-specific progerin expression provokes contractile impairment in a mouse model of Hutchinson-Gilford Progeria syndrome that is ameliorated by nitrite treatment. *Cell* **9**, 656 (2020).
73. L. Del Campo, M. Ferrer, Wire myography to study vascular tone and vascular structure of isolated mouse arteries. *Methods Mol. Biol.* **1339**, 255–276 (2015).
74. C. Galán-Arriola, J. P. Vílchez-Tschischke, M. Lobo, G. J. López, A. de Molina-Iracheta, C. Pérez-Martínez, R. Villena-Gutiérrez, Á. Macías, I. A. Díaz-Rengifo, E. Oliver, V. Fuster, J. Sánchez-González, B. Ibanez, Coronary microcirculation damage in anthracycline cardiotoxicity. *Cardiovasc. Res.* **118**, 531–541 (2022).
75. S. Kalinovic, M. Oelze, S. Kröller-Schön, S. Steven, K. Vujacic-Mirski, M. Kvandová, I. Schmal, A. Al Zuabi, T. Münzel, A. Daiber, Comparison of mitochondrial superoxide detection ex vivo/in vivo by mitoSOX HPLC method with classical assays in three different animal models of oxidative stress. *Antioxidants* **8**, 514 (2019).
76. J. Zielonka, S. Srinivasan, M. Hardy, O. Ouari, M. Lopez, J. Vasquez-Vivar, N. G. Avadhani, B. Kalyanaraman, Cytochrome c-mediated oxidation of hydroethidine and mito-hydroethidine in mitochondria: Identification of homo- and heterodimers. *Free Radic. Biol. Med.* **44**, 835–846 (2008).
77. J. Zielonka, J. Vasquez-Vivar, B. Kalyanaraman, Detection of 2-hydroxyethidium in cellular systems: A unique marker product of superoxide and hydroethidine. *Nat. Protoc.* **3**, 8–21 (2008).
78. E. Bonzon-Kulichenko, E. Camafeita, J. A. López, M. Gómez-Serrano, I. Jorge, E. Calvo, E. Núñez, M. Trevisan-Herraz, N. Bagwan, J. A. Bárcena, B. Peral, J. Vázquez, Improved integrative analysis of the thiol redox proteome using filter-aided sample preparation. *J. Proteomics* **214**, 103624 (2020).
79. S. Martínez-Bartolomé, P. Navarro, F. Martín-Maroto, D. López-Ferrer, A. Ramos-Fernández, M. Villar, J. P. García-Ruiz, J. Vázquez, Properties of average score distributions of SEQUEST: The probability ratio method. *Mol. Cell. Proteomics* **7**, 1135–1145 (2008).
80. P. Navarro, J. Vázquez, A refined method to calculate false discovery rates for peptide identification using decoy databases. *J. Proteome Res.* **8**, 1792–1796 (2009).
81. M. Trevisan-Herraz, N. Bagwan, F. García-Marqués, J. M. Rodriguez, I. Jorge, I. Ezkurdia, E. Bonzon-Kulichenko, J. Vázquez, SanXoT: A modular and versatile package for the quantitative analysis of high-throughput proteomics experiments. *Bioinformatics* **35**, 1594–1596 (2019).
82. F. García-Marqués, M. Trevisan-Herraz, S. Martínez-Martínez, E. Camafeita, I. Jorge, J. A. Lopez, N. Méndez-Barbero, S. Méndez-Ferrer, M. A. Del Pozo, B. Ibáñez, V. Andrés, F. Sánchez-Madrid, J. M. Redondo, E. Bonzon-Kulichenko, J. Vázquez, A novel systems-biology algorithm for the analysis of coordinated protein responses using quantitative proteomics. *Mol. Cell. Proteomics* **15**, 1740–1760 (2016).
83. P. Martínez-Acedo, E. Núñez, F. J. Sánchez Gómez, M. Moreno, E. Ramos, A. Izquierdo-Álvarez, E. Miró-Casas, R. Mesa, P. Rodriguez, A. Martínez-Ruiz, D. G. Dorado, S. Lamas, J. Vázquez, A novel strategy for global analysis of the dynamic thiol redox proteome. *Mol. Cell. Proteomics* **11**, 800–813 (2012).
84. J. B. Spinelli, P. C. Rosen, H. G. Sprenger, A. M. Puszynska, J. L. Mann, J. M. Roessler, A. L. Cangelosi, A. Henne, K. J. Condon, T. Zhang, T. Kunchok, C. A. Lewis, N. S. Chandel, D. M. Sabatini, Fumarate is a terminal electron acceptor in the mammalian electron transport chain. *Science* **374**, 1227–1237 (2021).

Acknowledgments: We thank S. Bartlett for editing and M. Rincón for the MCJ^{KO} mice. Microscopy was conducted at the Microscopy and Dynamic Imaging Unit at CNIC. We are grateful to O. G. Sáez, V. L. Cantarero, and E. Arza Cuesta for all the support in the acquisition and analysis of microscopy images. We thank A. Efeyan for providing the rapamycin special

diet. Biomedical imaging has been conducted at the Advanced Imaging Unit of the CNIC (Centro Nacional de Investigaciones Cardiovasculares Carlos III), Madrid, Spain. We thank Electron Microscopy Facility [Centro Nacional de Biotecnología (CSIC)] for preparing samples (Epon embedding), obtaining the ultrathin sections and transmission electron microscopy visualization. We thank the staff at the CNIC Animal Facility. **Funding:** This study was financially supported by the following: Interacciones celulares y sistémicas entre el cáncer y la señalización metabólica, exp: RED2022-134397-T (G.S.); Proyectos I+D+i 2019 - Proyecto MINECO-PID2019-104399RB-I00 financiado por MCIN/AEI/10.13039/501100011033 (G.S.); Proyectos de I+D de Generación de Conocimiento 2018 funded by Ministerio de Economía y Competitividad (PGC2018-097019-B-I00) (G.S.); PreMed-Exp: PMP21/00057 (G.S.); Fundación Jesús Serra (G.S.); EFSD/Lilly European Diabetes Research Programme (G.S.); BBVA Foundation Leonardo Grants program for Researchers and Cultural Creators (Investigadores-BBVA-2017) (G.S.); Fundación AECC PROYE19047SABI (G.S.); Comunidad de Madrid IMMUNOTHERCAN-CM S2010/BMD-2326 (G.S.); FPI Severo Ochoa CNIC program (BES-2016-077635) (A.M.S.); JDC-2020 Incorporación (IJC2020-042679-I) (P.H.-A.); Fondo Europeo de Desarrollo Regional (FEDER) Instituto de Salud Carlos III-Fondo de Investigación Sanitaria PI17/00995 (A.G.-Á.); Fondo Europeo de Desarrollo Regional (FEDER) Instituto de Salud Carlos III-Fondo de Investigación Sanitaria (PI20/00742) (A.G.-Á.); Intensificación AES2019 (AGA); Fundación "La Caixa": Macromoleculopathies (LCF/PR/HR19/52160013) of the call HEALTH RESEARCH 2018 (Á.Ma.); Programa de Atracción de Talento (2017-T1/BMD-5185) funded by Comunidad de Madrid (E.O.); Ramón y Cajal grant (RYC2020-028884-I) funded by MCIN/AEI/10.13039/501100011033 and by "ESF Investing in your future" (E.O.); Juan de la Cierva Incorporación Grant (IJCI-2016-27698) (M.V.O.); Worcester Foundation for Biomedical Research (J.B.S.); Boehringer Ingelheim Foundation (collaborative research group "Novel and neglected cardiovascular risk factors: molecular mechanisms and therapeutics") (A.D.); Foundation Heart of Mainz (A.D.); DZHK (German Center for Cardiovascular Research), Partner Site Rhine-Main, Mainz, Germany (A.D.); Ministerio de Ciencia e Innovación (PGC2018-097019-B-I00, PID2021-122348NB-I00, PLEC2022-009235, and PLEC2022-009298) (J.V.); Fundación "La Caixa" (HR17-00247 and HR22-00253) (J.V.); Carlos III Institute of Health-Fondo de Investigación Sanitaria grant PRB3 (PT17/0019/0003- ISCIII-SGEFI/ERDF, ProteoRed) (J.V.); and Comunidad de Madrid (IMMUNO-VAR, P2022/BMD-7333) (J.V.). The CNIC is supported by the Instituto de Salud Carlos III (ISCIII), the Ministerio de Ciencia e Innovación (MCIN), and the Pro CNIC Foundation and is a Severo Ochoa Center of Excellence (grant CEX2020-001041-S funded by MICIN/AEI/10.13039/501100011033). **Author contributions:** Methodology: G.S., A.M.S., B.C., S.R., Á.Ma., J.A.L., E.O., E.R., M.Leó., M.V.-O., A.G.-Á, B.I., J.V., J.B.S., A.D., and M.Lei. Investigation: G.S., A.M.S., E.O., S.F.R., Á.Ma., E.R., L.L., A.P.C., J.A.L., A.Mo., I.G.L., A.G.-Á, J.B.S., P.V., M.J., A.D., S.R., B.C., M.C., M.Lei., V.I.P., and J.V. Visualization: A.M.S., S.R., Á.Ma., A.G.-Á, J.A.B., B.I., J.V., E.O., and G.S. Funding acquisition: G.S. and A.D. Project administration: G.S., A.M.S., and J.B.S. Resources: B.C., P.H.-A, S.R., P.V., M.J., J.A.L., A.P.C., V.I.P., J.A.B., E.O., G.S., and B.I. Supervision: G.S., S.R., and A.G.-Á. Conceptualization: G.S., A.M.S., P.H.-A, Á.Ma., M.V.-O., A.G.-Á, V.I.P., and E.O.. Validation: G.S., A.M.S., S.R., P.V., M.J., Á.Ma., L.L., M.V.-O., A.G.-Á, V.I.P., and B.I.. Formal analysis: A.M.S., SRa, P.V., M.J., Á.Ma., J.A.L., M.Lei., J.V., and AD. Data curation: P.V., M.J., and B.I. Writing—original draft: G.S. and A.M.S. Writing—review and editing: G.S., A.M.S., E.O., Á.Ma., A.Mo., I.G.L., A.G.-Á, P.V., A.D., S.R., P.H.-A., J.A.B., B.I., and J.V. **Competing interests:** G.S. has received funding through Mitotherapeutix. All other authors declare that they have no competing interests. **Data and materials availability:** All data needed to evaluate the conclusions in the paper are present in the paper and/or the Supplementary Materials.

Submitted 5 September 2023
Accepted 19 December 2023
Published 19 January 2024
10.1126/sciadv.adk6524